

## Article

# Microfabrics, In Situ Trace Element Compositions of Pyrite, and the Sulfur Isotope Chemistry of Sulfides from the Xitieshan Pb-Zn Deposit, Qinghai Province, Northwest China: Analysis and Implications

Hui Yang  and Huashan Sun

School of Earth Resources, China University of Geosciences, Wuhan 430074, China

\* Correspondence: huiyangcug@126.com

**Abstract:** The Xitieshan deposit, located in the central segment of the northern margin of the Qaidam Basin, is among the largest massive Pb-Zn sulfide deposits in China. This deposit, along with its ore-bearing rock series known as the Tanjianshan Group, underwent greenschist facies metamorphism due to subsequent orogeny. We investigated the in situ sulfur isotopes of sulfides with different occurrences to define the origin of ore-forming fluids. The  $\delta^{34}\text{S}$  values of sulfides from stratiform ores, massive ores in schist, stockwork ores in marble, schist and discolored altered rocks that constitute a typical double-mineralization structure range from  $-5.3\text{‰}$  to  $+5.6\text{‰}$  and from  $-1.7\text{‰}$  to  $+32\text{‰}$ , respectively, indicating distinct biological and thermochemical reductions in seawater sulfates. These are similar to the sulfur isotopic characteristics of VSHMS deposits. Pyrite, whose LA-ICP-MS trace element compositions can provide significant information about metallogenic evolution and deposit genesis, is ubiquitous throughout the whole mineralization process. In these stratiform, massive and stockwork ores, three pyrite types were identified: colloform pyrite (Py0), fine-grained anhedral spongy pyrite (Py1) and coarse-grained euhedral pyrite (Py2). The contents of most metallogenic elements, such as Cu, Pb, Zn, Ag, Mo, Mn and Sn, decrease from Py0 to Py2 with the enhancement of metamorphic recrystallization. This suggests that the expelled elements appear as inclusions in primitive pyrite, contributing to the precipitation of new sulfide phases, such as sphalerite and galena. Orogenic metamorphism played an important role in controlling further Pb-Zn enrichment of the Xitieshan deposit. Moreover, there is another mineralization type, primarily occurring as sulfide veins in the undeformed Formation C siltstones of the Tanjianshan Group, which also crosscut early-formed sulfides, showing close-to-zero S isotopic compositions. In this mineralization type, pyrite (Py3) displays high Se/Tl ( $>10$ ) and Co/Ni ( $>2.2$ ) ratios, both indicating a minor superimposed post-orogenic magmatic–hydrothermal event.



**Citation:** Yang, H.; Sun, H. Microfabrics, In Situ Trace Element Compositions of Pyrite, and the Sulfur Isotope Chemistry of Sulfides from the Xitieshan Pb-Zn Deposit, Qinghai Province, Northwest China: Analysis and Implications. *Minerals* **2023**, *13*, 1549. <https://doi.org/10.3390/min13121549>

Academic Editors: Pura Alfonso, Panagiotis Voudouris, Yucai Song, Stylianos Tombros and Degao Zhai

Received: 1 October 2023

Revised: 7 December 2023

Accepted: 12 December 2023

Published: 15 December 2023



**Copyright:** © 2023 by the authors. Licensee MDPI, Basel, Switzerland. This article is an open access article distributed under the terms and conditions of the Creative Commons Attribution (CC BY) license (<https://creativecommons.org/licenses/by/4.0/>).

**Keywords:** Xitieshan Pb-Zn deposit; in situ microanalysis; trace element; sulfur isotope; metallogenesis; pyrite

## 1. Introduction

Massive sulfide deposits, commonly distributed in marine volcanic or sedimentary sequences, constitute a significant global source of Pb, Zn, Cu, Au and Ag, as well as other metals, such as Se, Sn, Mn, Co, Cd, In, Ga, Ge and Bi [1,2]. This is well understood in numerous extant studies on ancient deposits and present-day seafloor analogues [3,4]. In the case of ancient massive sulfide deposits situated in orogenic environments, most undergo different degrees of metamorphism and deformation [5,6], giving rise to the reactivation, migration and reprecipitation of metals [7–9]. Therefore, there are generally two or more mineralized stages in these deposits: syngenetic seafloor hydrothermal mineralization and superimposed modified mineralization associated with metamorphism or tectonic magmatism [10–13]. However, it has always been difficult to establish methods of identifying these

different metallogenic types, determining their distinct contributions to the final deposit and analyzing the complete process in research into these varieties of deposit.

The Xitianshan deposit, located in the central segment of the northern margin of Qaidam Basin in NW China, is among the largest Pb-Zn deposits in China, with a metal reserve of 64 Mt at an average grade of 4.86% Zn, 4.16% Pb, 0.68 g/t Au and 58 g/t Ag [14]. The host rocks of the deposit are composed of a series of submarine volcanic and subvolcanic rocks, interbedded with sedimentary sequences formed in a back-arc basin setting [15–17], which have generally been affected by metamorphism. These varieties of rock include greenschist facies regionally and amphibolite facies locally [14,18,19]. The genesis of the Xitianshan deposit has long been controversial. This includes efforts to classify the SEDEX genetic type [20–23], VMS type [24,25] or VSHMS type, displaying transitional features between SEDEX and VMS deposits [14,17,26]. Moreover, little or no research has been conducted on the complete mineralization process of the Xitianshan deposit. It is necessary to investigate the signature of its original submarine mineralization, the specific mechanism of influence on the composition of ores, the mobilization of metals due to metamorphism, and a minor post-orogenic overprinted magmatic–hydrothermal event that occurred in this deposit and which has never been reported previously.

The Xitianshan deposit provides a unique opportunity to investigate geological and geochemical features and the entire ore-forming process of syngenetic massive sulfide deposits hosted in an orogenic belt. Although the trace element and sulfur isotopic compositions of pyrite have been studied [25], the classification of upper sedimentary and lower stockwork structures in a submarine hydrothermal system of the deposit is lacking, and our understanding of the types of mineralization is far from sufficient. Therefore, based on more detailed fieldwork and ore microscopy studies, in combination with an LA-ICP-MS microanalysis, we performed an in situ sulfur isotopic analysis of sulfides from distinct mineralization types and a trace elemental analysis of different generations of pyrite from the Xitianshan deposit to determine Pb-Zn mineralization. In this paper, we attempt to (1) reconstruct the influence of the process of metamorphism and (2) determine the source of sulfur in this deposit.

## 2. Geological Background

### 2.1. Regional Geology

The northern margin of the Qaidam basin (NMQB), situated in the northeast of the Qinghai–Tibet Plateau (Figure 1), is a typical compound collision orogenic belt, experiencing episodic geotectonic evolution processes including oceanic subduction (>440 Ma), continental collision (440–420 Ma), crustal exhumation (420–390 Ma) and final orogen collapse (390–360 Ma) in the early Paleozoic, along with the formation of ultra-high-pressure metamorphic (UHPM) rocks [27–29]. The belt extends in a NW–SE direction and is approximately 700 km long and 30–60 km wide [25]. It is primarily composed of the Oulongbuluke microplate in the north and the North Qaidam (NQD) orogenic belt in the south, being separated by the regional NW-striking Ulan–Yuqia Fault (Figure 1). The Oulongbuluke is the oldest microblock in this belt, displaying a double-layered basement–cover structure with weak magmatism [17], with the basement composed of the Precambrian Delingha complex, Dakendaban Group and Wandonggou Group, which are in tectonic contact with each other [30], and the cover composed of the Nanhua–Sinian QuANJI Group with a zircon U–Pb age of 738 Ma in its lower basalt [31,32]. Conversely, the crystalline basement of the NQD orogenic belt mainly consists of the Meso- and Neoproterozoic Dakendaban Group gneiss, which is overlain by the lower Paleozoic Tanjianshan Group metamorphic marine-facies volcano-sedimentary rocks and the upper Paleozoic–Mesozoic sedimentary sequence. The well-known Yukahe–Shaliuhe HP–UHP metamorphic belt, located at the margin of the NQD, mainly comprises granitic and pelitic gneiss with intercalated eclogite and/or garnet peridotite. Generally speaking, the emplacement of Paleozoic granite in NMQB occurred in four periods: 465–473, 440–446, 397–408 and 372–383 Ma [28]. The NMQB is metallogenically fertile, hosting different types of deposits such as the Yuka and

Tanjianshan orogenic Au, Lvliangshan massive sulfide Cu, Shuangkoushan vein Pb-Zn-Ag and the Xitieshan Pb-Zn deposits [33–36]. Among these, there are two gold hydrothermal mineralized events (409.4 Ma and 288.0~268.9 Ma) in the Tanjianshan Au deposit [33], while the metallogenic ages of the Yuka Au and Shuangkoushan Pb-Zn deposits are 376.9 Ma [37] and 347–362 Ma [38], respectively.

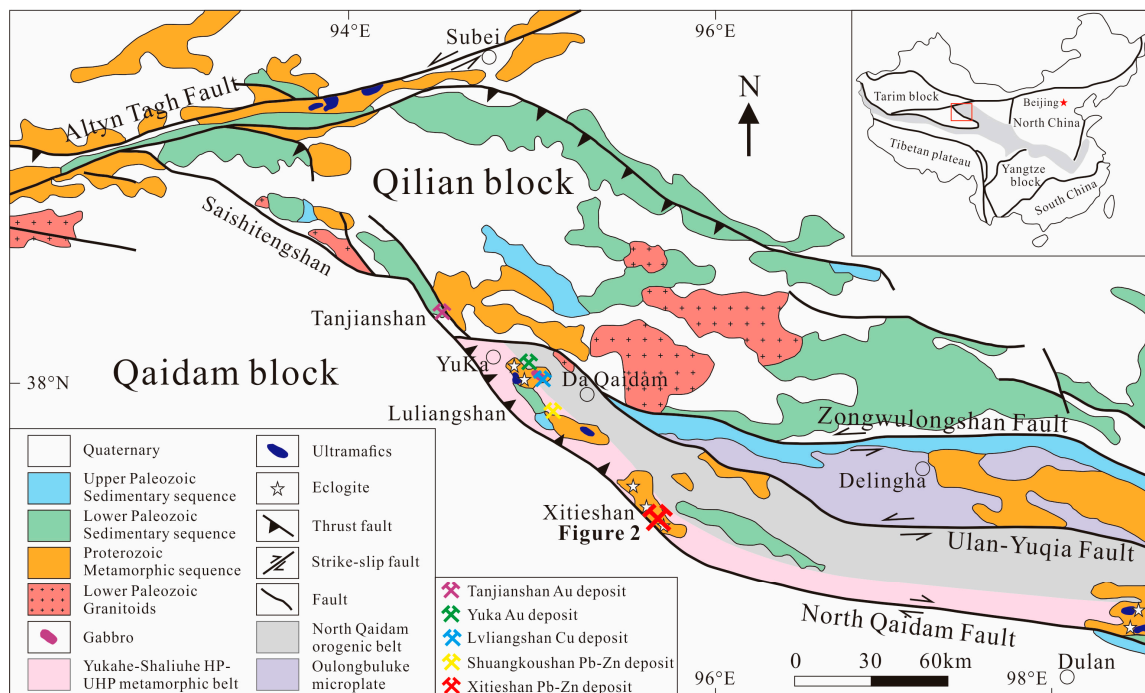


**Figure 1.** Geological map of the northern margin of the Qaidam basin, Northwest China [39]. The location of the Xitieshan Pb-Zn deposit (Figure 2) is marked with red X.

## 2.2. Geology of the Xitieshan Deposit

From north to south, outcropped strata in the Xitieshan mining area predominantly include the Shaliuhe Group, the Tanjianshan Group, and a small part of the Amunike, Chengqianggou and Ganchaigou Formations (Figure 2). The Shaliuhe Group is a major component of the UHP metamorphic belt [19], which is primarily composed of eclogite, gneiss, schist and retrograded amphibolite [40], and which is in fault contact with the Ordovician Tanjianshan group that hosts the massive sulfide orebodies. Further, it is traditionally divided into A, B, C and D formations. Of which, Formation A is subdivided into two sections, namely, A-1 and A-2, with the former characterized by a metamorphosed bimodal volcanic composition with an early–middle Ordovician age (464.6 Ma [24],  $486 \pm 13$  Ma [41], 458–463 Ma [42], 452–461 Ma [14]) and the latter dominated by metasedimentary rocks, including marble and carbonaceous chlorite quartz schist, constituting the main ore-bearing layer. Additionally, Formation B is the minor ore-bearing layer, consisting of sericite quartz schist and carbonatized plagioclase chlorite schist. Formation C is composed of a variety of purple-red sandstone and polymictic gravel-bearing sandstone interbedded with lesser conglomerates, which has been excluded from the Tanjianshan Group as a product of postcollisional foreland basin sedimentation [17,43,44]. Formation D is primarily composed of metamorphosed basic volcanic rocks with subordinate metasedimentary rocks, further subdivided into four sections: metamorphosed basic volcanoclastic rocks and lavas (Section D-1), metasedimentary rocks including sericite quartz schist and thin marble (Section D-2), meta-basalt and meta-basaltic andesite (Section D-3), and plagioclase amphibolite schist and chlorite schist (Section D-4). The transformation of geochemical signatures in volcanic rocks from Formations A to D indicates the development of a back-arc basin in a continental margin, with continuous extension and spreading [16].

In addition, the overlying Devonian Amunike, Carboniferous Chengqianggou and Triassic Ganchaigou Formations consist of a set of undeformed aubergine sandstone, conglomerate and yellowish coarse-grained feldspar quartz sandstone, as well as glutenite, sandstone and mudstone, respectively.

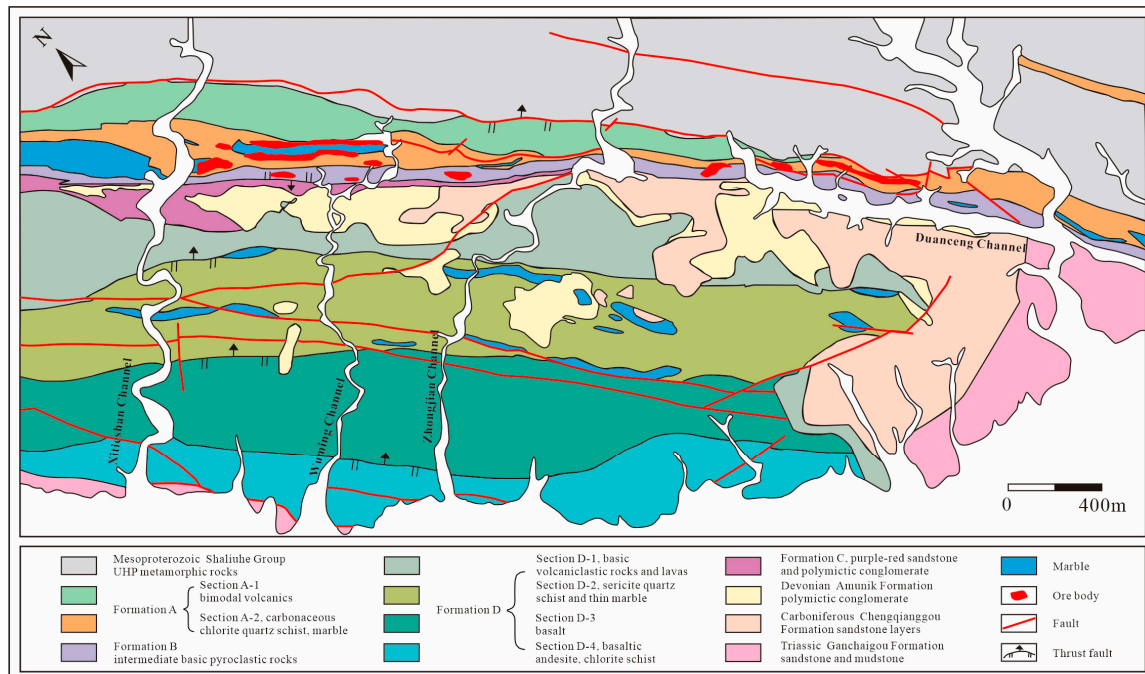


**Figure 2.** Geological map of the Xitieshan deposit [42].

The volcano-sedimentary rocks of the Tanjianshan Group (except Formation C) have undergone greenschist- to amphibolite-facies deformation and metamorphism, producing a metacryst assemblage of chlorite, epidote, amphibole, actinolite, zoisite, albite, sericite and quartz [17]. Previous investigations of the structural geology at Xitieshan have revealed a two-episode deformational history (early main ductile and late brittle deformation) [30]. Ductile deformation is widely visible in the Tanjianshan Group, represented by penetrative schistosity, dissymmetric Z-shaped folds, recumbent folds, tight folds, rootless intrafolial folds, boudinage and mullion structures. The  $^{40}\text{Ar}$ - $^{39}\text{Ar}$  age of muscovite in the granitic mylonitic gneiss from the Xitieshan ductile shear zone is 406~400 Ma [45], indicating the likely association between formation and crustal exhumation. By comparison, brittle deformation is featured by a battery of thrust faults, kink bands and shear fractures superimposed onto the earlier ductile deformation. In addition, four major episodes of Paleozoic granitic magmatism in the North Qaidam Basin can be recognized. These are 473–465, 446–440, 408–391, and 386–360 Ma, respectively, values that are related to different orogenic processes such as oceanic plate subduction, continental collision, exhumation and orogen collapse [28,29,46].

### 2.3. Orebody and Alteration

In the Xitieshan orefield, the orebodies are lenticular or banded, with discontinuous distribution in the Tanjianshan Group along the strike (NW-SE), which extends for around 5~6 km with a width of about 60~200 m (Figure 2). The footwalls of the sulfide ore bodies comprise metamorphic bimodal volcanic rocks (Figure 3a,b), with several layers of thin bedded jasper and siliceous rocks exposed at the top of the ore-bearing layers, while the upper parts of the sulfides are meta-basic volcanic rocks of the D Formation.

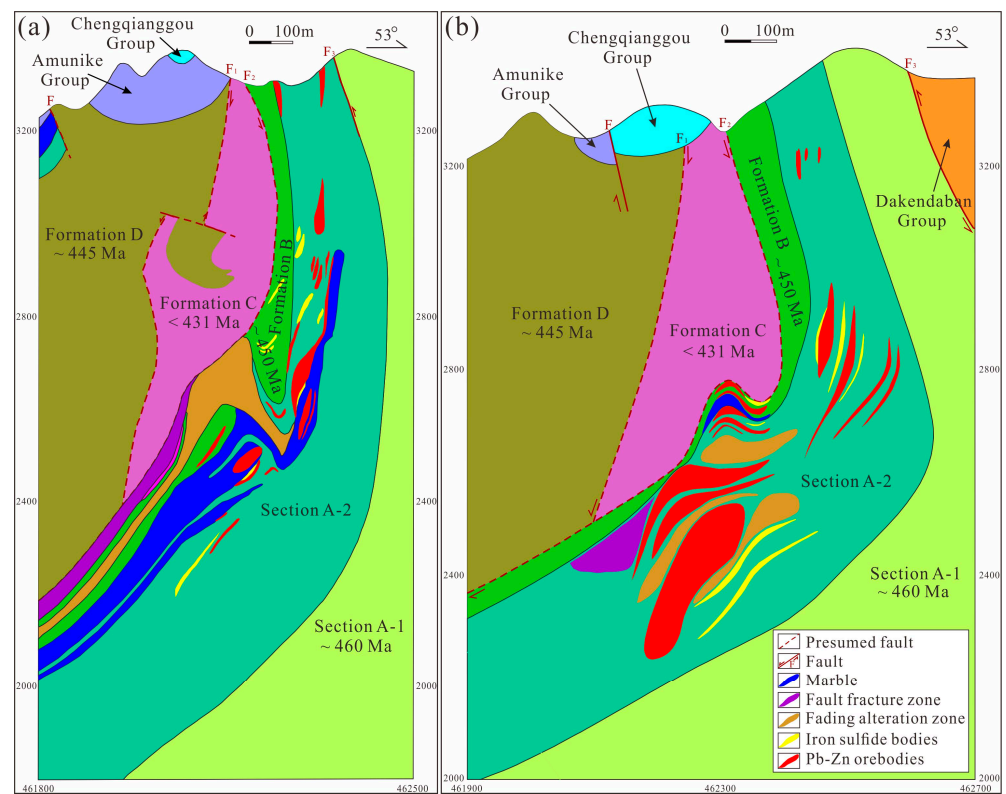


**Figure 3.** Geological section along (a) 1 exploration line (modified after [47]) and (b) 07 exploration lines (modified after [48]) of the Xitianshan deposit. The ages of the volcanic rocks from Section A-1, Formation D are from [42]; the age of the volcanic rocks from Formation B is from [14]; and the age of the sedimentary rocks from Formation C is from [44].

Other studies have used two principal classifications of ore bodies in the Xitianshan deposit, one of which is based on the shape of orebodies [25], while the other is based on the type of wall rocks [40]. In order to represent the upper sedimentary and lower stockwork structures of the Xitianshan deposit visually and pellucidly, we classify the sulfide mineralization via a combination of the above two methods, designating two major types according to the relationship between ore bodies and country rocks (Figure 4): an economically significant stockwork-type mineralization (more than 80% of the total reserves) located in the lower middle part of Section A-2 and Formation B; and an economically less stratiform-type mineralization situated in the middle–upper part of the Section A-2.

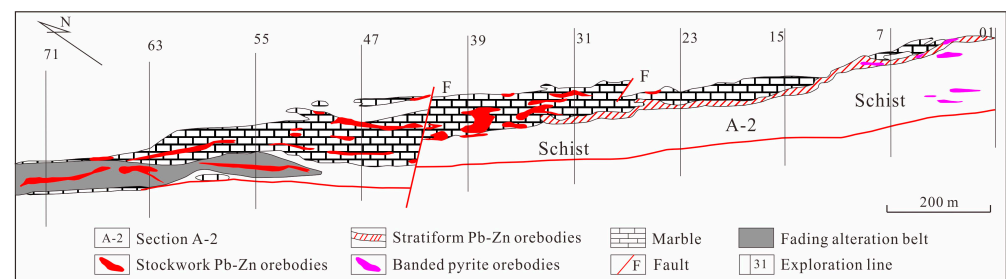


**Figure 4.** Geological map of 2942 m level in the Xitianshan deposit (modified after [22]).

Barite veins are locally distributed throughout the upper part of the sulfide ore bodies (Formation D; Figure 5a). The surrounding rocks of the stockwork-type mineralization consist of marble, schist and discolored strongly altered rocks. The orebodies in marble constitute the primary portion of stockwork-type mineralization. These primarily dip SW, locally dip NE with a steep dip angle, and are characterized by veined, irregular

(Figure 5b,c) shapes without obvious deformation, displaying sharp and discordant contact boundaries with the host marble. Coarse-grained recrystallized calcites composed of bleached sucrosic marble were locally observed at the edge of the sulfide veins (Figure 5d), probably reflecting fluid–marble interaction. Variable-sized and collageable breccias of marble, cemented by sulfide minerals (Figure 5e), were also discovered in this type of mineralization. Nevertheless, stringer and disseminated sulfides are commonly intergrown (Figure 5f) in the stockwork orebodies from schist, showing relatively stronger surrounding rock alterations, including silicification, pyritization, carbonatation and sericitization. Among these alterations, silicification and pyritization are the most widespread and closely associated with Pb–Zn mineralization. Moreover, it is worth noting that there is a discolored, strongly altered belt distributed in schist-type mineralized zones (Figure 3a,b). This has never been specially reported and has not received enough attention previously. Ore minerals primarily occur as disseminated grains or veins in these gray-to-white altered rocks (Figure 5g,h).

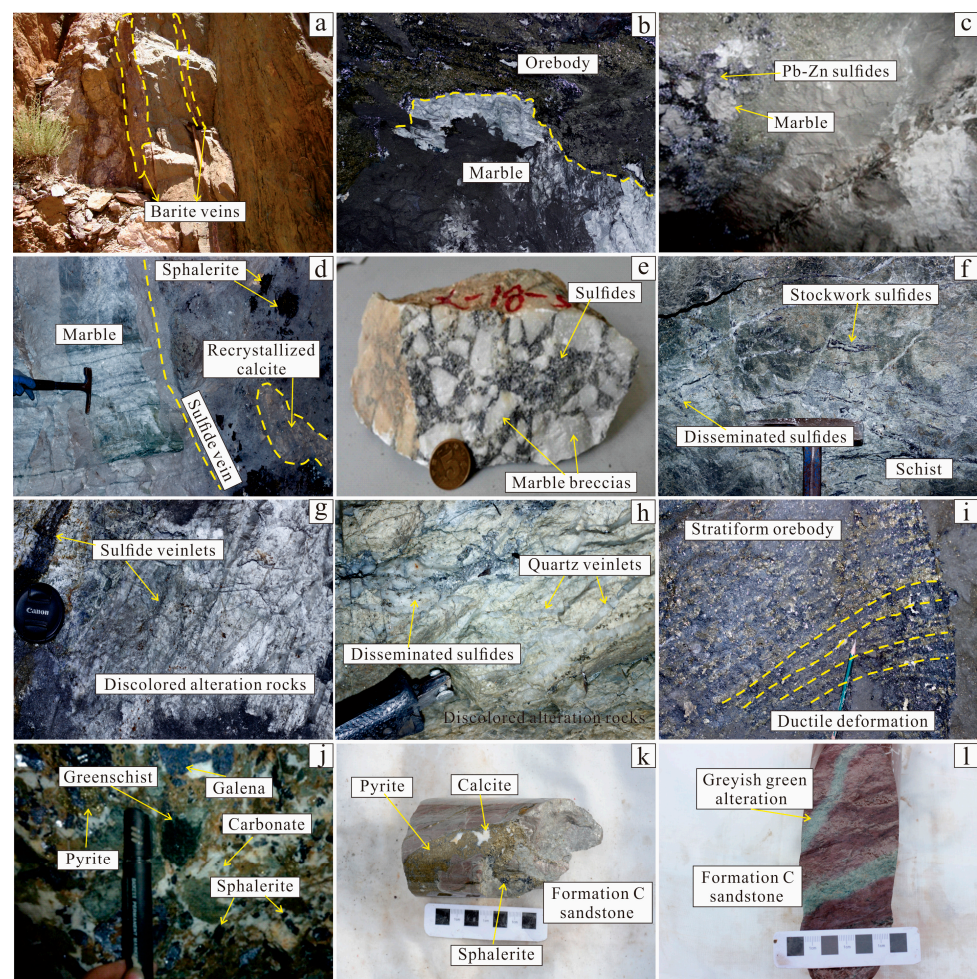


**Figure 5.** Outcrop and ore photographs showing Pb–Zn mineralization in the Xitianshan deposit. (a) Barite veins in the schists; (b) sulfide orebody in host marble composed of sphalerite, pyrite and galena; (c) granophyric sulfide orebody in host marble; (d) sulfide vein crosscuts the laminar marble; (e) collageable fragments marble cemented by pyrite, sphalerite, galena and carbonate; (f) stockwork and disseminated sulfides in host schist; (g) sulfide stockworks in the host discolored alterations rocks; (h) disseminated sulfides and quartz veinlets in the host discolored alterations rocks; (i) co-folded stratiform orebody including sphalerite and pyrite; (j) multi-components, angular and variable-sized fragments of galena, sphalerite, pyrite cemented by carbonate; (k) pyrite vein in the host Formation C siltstone; (l) greyish-green alteration on both sides of sulfide vein in the host Formation C siltstone.

Conversely, the host rock of the stratiform-type mineralization is mainly schist (Figure 4), whether carbonaceous schist, chlorite quartz schist or sericite quartz schist. In the cross-section, the main orebody of this mineralization type is distributed in a nearly parallel manner to the strata, which strikes northwest and dips to the northeast (Figure 3b). The stratiform ores are absolutely restrained by the stratigraphy of the host schist, consisting of sheet-like sulfide-rich layers (Figure 5i) or being interbedded with schist or silicalite, each of which is co-folded in accordance with the schistosity and foliation. Occasionally, multi-component breccias comprising angular fragments of silicalites, greenschists and ores are cemented by carbonate minerals (Figure 5j). Generally, deformation textures such as cataclastic, directional, fracture healing and corrugation are more common in schist-hosted ores than marble-hosted ores, which can be attributed to the strong capacity of marble to protect inner orebodies weakly affected by orogenic metamorphism [9,40].

In addition to the above two primary styles of mineralization, there is another minor style of mineralization characterized by sulfides. This is mainly composed of pyrite, with minor quantities of sphalerite and galena crosscutting the sandstone of Formation C (Figure 5k). As mentioned above, Formation C sedimentary rocks were considered to be products of post-collisional foreland basin sedimentation, with weakly or no metamorphic and deformation features. Furthermore, there is a transformation of color from aubergine in country sandstones to a greyish green in the margin of sulfide veins (Figure 5l). The deformation and wall rock alteration characteristics of these veined pyrite mineralizations were more distinct in Formation C than in the two major metallogenic (marble and schist) types, revealing that this mineralized style probably represents the latest period (post-orogenic) of superimposed metallogenic event.

### 3. Ore Mineralogy and Petrography

Based on mineral paragenetic sequence, textural characteristics, crosscutting relationships and degrees of deformation, three main stages of mineralization in the Xitieshan deposit have been recognized (Figure 6), namely the early submarine hydrothermal mineralization stage (stage 1), the metamorphism and deformation stage (stage 2), and the late superimposed hydrothermal mineralization stage (stage 3).

Stage Minerals	Submarine hydrothermal mineralization	Metamorphism and deformation	Superimposed hydrothermal mineralization
Pyrite0	—		
Pyrite1	—		
Sphalerite1	—		
Galena1	—		
Pyrrhotite1	—		
Pyrite2		—	
Sphalerite2		—	
Galena2		—	
Pyrrhotite2		—	
Pyrite3			—
Quartz	—	—	
Calcite			—
Muscovite		—	

**Figure 6.** Simplified paragenetic sequence of mineralization at the Xitieshan deposit.

Stage 1 was characterized by the initial colloform pyrite (Py0) that was mainly observed in the stratiform or massive orebodies, typically showing a concentric ring texture with many small pores in the surface filled by clay or other minerals (Figure 7a), and subsequent fine-grained anhedral spongy sulfides composed of pyrite (Py1), sphalerite (Sp1), galena (Gn1) and pyrrhotite (Po1). These porous sulfides mostly occur as bedding-parallel bands intercalated with siliceous rock. In this study, these were classified as Py1a (Figure 7b), Sp1a and Gn1a (Figure 7c), respectively, showing submarine sedimentary signatures for their grain size, degree of crystallization and laminar occurrence. Occasionally, the concentrated laminae of anhedral spongy pyrite are also accompanied by anhedral porous pyrrhotite aggregates (Figure 7d). Another appearance of these porous sulfides was as veinlets or disseminated grains distributed in the distinct fading alteration belt. These were listed as Py1b and Sp1b (Figure 7e), representing the altered stockwork belt of the seafloor hydrothermal system [21]. In massive ore rocks, colloform pyrite was generally surrounded by spongy pyrite or pyrrhotite and both were replaced by porous sphalerite (Figure 7f).

Stage 2 was characterized by the distinct texture of sulfides with euhedral shapes, clean surfaces, and larger grain sizes, which were classified as Py2, Sp2, Gn2 and Po2. Coarse-grained euhedral pyrite (Py2) occurs as discrete crystals with square or pyritohedral outlines near the colloform pyrite (Figure 7g) or as stratiform-like aggregates that are much more massive than bedded Py1 (Figure 7h). We also observed a huge porphyroblast of pyrite situated in the matrix of fine-grained spongy pyrrhotite and pyrite (Figure 7i). Additionally, growth zoning in pyrite and galena was discovered in some ore samples, ranging from inclusion-rich sieved cores to inclusion-free homogeneous rims (Figure 7j,k). Among the materials discovered, the pyrite grain with a core–rim structure was further crosscut later by a pyrite vein (Figure 7j). In addition, this type of sulfide was also featured by various deformation structures, including the anhedral rounded pyrite aggregates with crooked contact boundaries found in the matrix of pyrrhotite and sphalerite (Figure 7l) and the rhombus-shaped pyrites displaying typical  $120^\circ$  triple junctions (Figure 7m). In some rock samples, pyrite and sphalerite commonly possess a cataclastic texture, with fractures usually related to hydrothermal venation consisting of relatively later ductile galena, sphalerite (Figure 7n), and calcite (Figure 7o). Sometimes, it occurs that the galena is rounded into a subangular isolated grain located in the interstice of subhedral pyrite. This material displays a deformed texture characterized by micro-folds (Figure 7p), which is possibly due to layer-parallel compressive forces. Consistent with Py1, the coarse-grained euhedral pyrite appearing as laminated aggregates in massive or bedded ores was listed as Py2a, while that which appeared as veined or disseminated grains in the discolored alteration rocks was classified as Py2b.

Stage 3 was characterized by later vein-type sulfides (dominated by pyrite with minor other sulfides). These not only occurred in Formation C (Figure 7q), but also in the massive or stratiform orebodies that crosscut the colloform pyrite and porous pyrite, pyrrhotite and sphalerite (Figure 7r), or bedded anhedral spongy pyrite and pyrrhotite (Figure 7s), which were classified as Py3, showing inclusion-poor features. Additionally, this type of pyrite was found to cement homogeneous sphalerite breccias with calcite (Figure 7t).

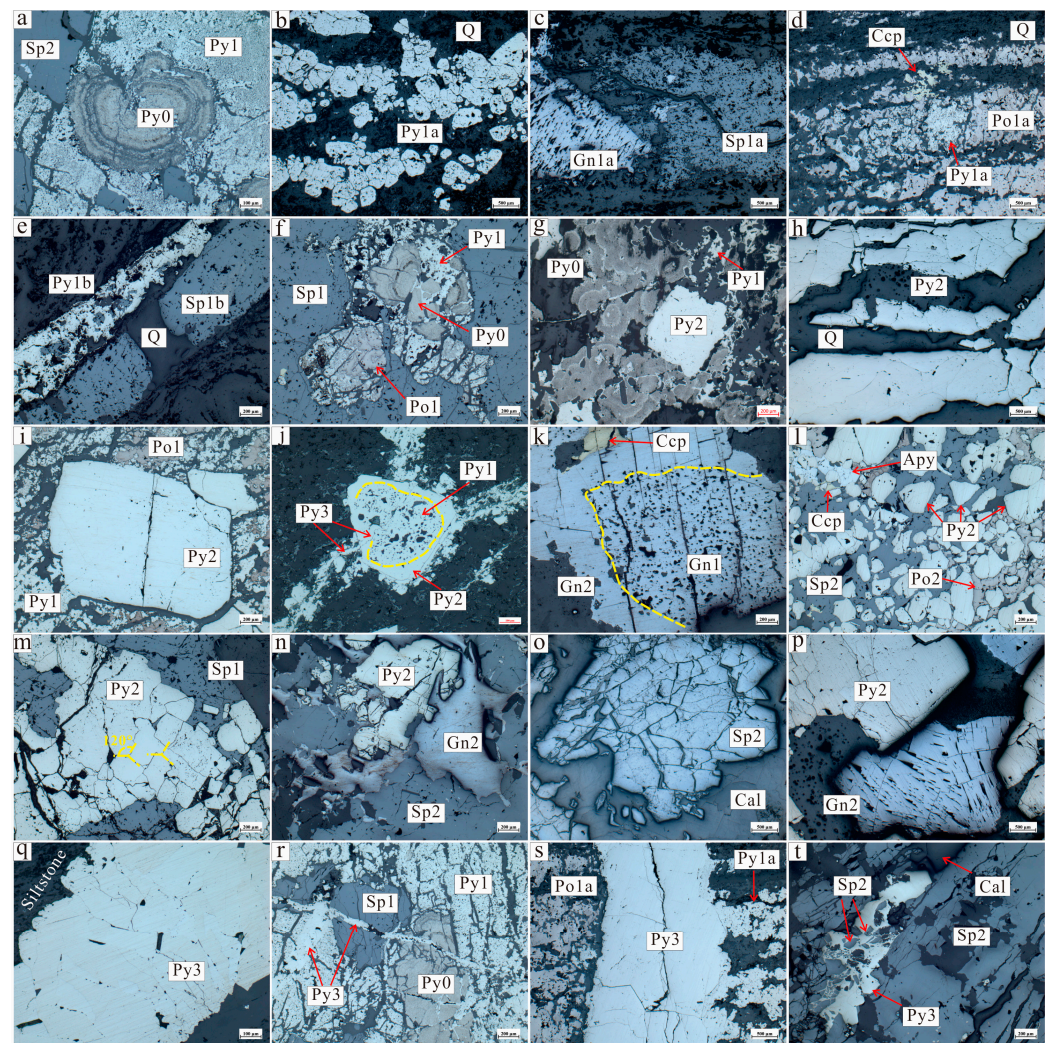


**Figure 7.** Photomicrographs (plane-polarized reflected light) illustrating sulfide minerals and textural characteristics of the Xitieshan deposit. (a) Colloform pyrite with concentric ring texture surrounded by anhedra spongy pyrite; (b) stratiform fine-grained anhedra spongy pyrite; (c) laminated anhedra porous sphalerite and galena; (d) layered fine-grained anhedra pyrite and pyrrhotite aggregates; (e) pyrite and sphalerite veins in the fading alteration rocks; (f) colloform and spongy pyrite were both replaced by porous sphalerite; (g) euhedral pyrite near the colloform pyrite; (h) stratiform-like recrystallized pyrite; (i) coarse-grained cubic pyrite porphyroblast in a matrix of anhedra spongy pyrrhotite and pyrite; (j) inclusion-rich pyrite crystal containing corroded core and overgrowth rim, both being crosscut by veined pyrite; (k) core–rim structure of galena; (l) anhedral rounded pyrite in the matrix of pyrrhotite and sphalerite; (m) recrystallized pyrite with typical  $120^\circ$  triple junctions; (n) cataclastic pyrite replaced and filled by sphalerite and galena; (o) cataclastic sphalerite filled with calcite; (p) micro-fold-deformed texture of galena; (q) later pyrite vein in Formation C siltstone; (r) colloform pyrite, spongy pyrite, pyrrhotite and sphalerite were crosscut by later pyrite vein; (s) later pyrite vein crosscut bedded spongy pyrrhotite, pyrite; (t) later pyrite vein cemented sphalerite breccias. Abbreviations: Py0 = colloform pyrite, Py1 = fine-grained spongy pyrite, Sp1 = anhedra porous sphalerite, Po1 = anhedra porous pyrrhotite, Gn1 = anhedra porous galena, Py1a = stratiform fine-grained spongy pyrite, Sp1a = stratiform porous sphalerite, Gn1a = stratiform porous galena, Po1a = bedded porous pyrrhotite, Py1b = veined fine-grained spongy pyrite, Sp1b = veined porous sphalerite, Py2 = coarse-grained euhedral pyrite, Sp2 = homogenous sphalerite, Gn2 = homogenous galena, Po2 = homogenous pyrrhotite, Py3 = late pyrite vein, Ccp = chalcopyrite, Apy = arsenopyrite, Q = quartz, and Cal = calcite.

#### 4. Sampling and Analytical Methods

More than 30 ore samples were collected from the mining surface, underground mine, and drill holes in the Xitieshan deposit. These areas generally contain all three mineralization types, which normally consist of four pyrite generations with distinct structures. Double-polished thin sections were prepared from these samples, and detailed petrographic observations of these sulfides, especially pyrite, were carried out. Subsequently, in situ LA-ICP-MS (laser ablation inductively coupled plasma mass spectrometer) S isotopic and trace element analyses were performed on typical sulfides from different metallogenic types and pyrites of different generations, respectively.

##### 4.1. Trace Elements in Pyrite

Trace element analysis of pyrite was conducted at Wuhan Sample Solution Analytical Technology Co., Ltd., using an Agilent 7900 quadrupole mass spectrometer coupled to a GeolasPro laser ablation system composed of a COMPexPro 102 ArF excimer laser and a MicroLas optical system, acting in accordance with the procedure of [49]. Helium acted as a carrier gas of the ablated materials during the experiment, while Argon was applied as a make-up gas, which was mixed with the carrier gas via a T-connector before entering the ICP. Analytical parameters were 32  $\mu\text{m}$  for spot size, 5 Hz for frequency and 5.5  $\text{J}/\text{cm}^2$  for laser energy. The total analysis time for each spot was approximately 70–80 s, including 20–30 s of a background acquisition and 50 s for the data acquisition from the sample. Various reference materials (NIST 610) were used as external calibration standards, albeit without an internal standard, to calibrate the trace element compositions of pyrite [50]. The sulfide reference material of MASS-1 (USGS) was analyzed to check analytical accuracy. Additionally, the trace element data were processed using the Excel-based software ICPMSDataCal, including the selection of background and analyzed signals, time-drift correction, and quantitative calibration [50]. The precision of analysis was monitored via the repeated analysis of the sulfide standards, yielding <15% RSD for most elements.

##### 4.2. S Isotopic Analyses

In situ sulfur isotope analyses were performed on pyrite taken from polished sections using a Nu Plasma II multi-collector inductively coupled plasma mass spectrometer (MC-ICP-MS) system equipped with a RESOLUTION S-155 193 nm ArF excimer laser ablation system, at the State Key Laboratory of Geological Processes and Mineral Resources (GPMR), China University of Geosciences, Wuhan. Helium was used as the carrier gas. During the experiment, the spot size and frequency were 33  $\mu\text{m}$  and 10 Hz, respectively, with the ablation process lasting for 40 s. Standard sample bracketing (SSB) was used to determine the  $\delta^{34}\text{S}$  ( $\delta^{34}\text{S} = ({}^{34}\text{S}/{}^{32}\text{S})_{\text{sample}}/({}^{34}\text{S}/{}^{32}\text{S})_{\text{V-CDT}} - 1$ ) values of the samples throughout the MC-ICP-MS analytical sessions. To calibrate the mass bias for sulfur isotopes, an international sphalerite standard NBS-123 ( $\delta^{34}\text{S}_{\text{V-CDT}} = +17.1\text{‰}$ ) and an in-house pyrite standard named WS-1, which is a natural pyrite crystal from the Wenshan polymetallic skarn deposit in Yunnan Province in South China, were analyzed repeatedly. The  $\delta^{34}\text{S}_{\text{V-CDT}}$  values ( $+1.1\text{‰} \pm 0.2\text{‰}$ ) of WS-1 were determined via secondary ion mass spectrometry (SIMS) at the Chinese Academy of Geochemistry, Guangzhou [51]. The analysis results were corrected for use in instrumental mass fractionation using a linear interpolation between two neighboring standards. The  $2\sigma$  analytical error was estimated to be  $\pm 0.3\text{‰}$ .

#### 5. Results

##### 5.1. Trace Element Compositions of Pyrite

A total of 90 LA-ICP-MS spot analyses were performed on samples from mine, surface and drill holes, including 18 spots on Py0, 27 spots on Py1, 32 spots on Py2, and 13 spots on Py3. The results of the in situ trace element analyses of the four pyrite types are listed in Table 1. The dataset displays wide ranges in pyrite trace element chemistry among the Xitieshan deposits, which are common in LA-ICP-MS studies due to several modes

of element occurrences and complex formation mechanisms of pyrite. Summary analyses of different types of pyrite for certain elements (Co, Ni, As, Sb, Tl, Au, Cu, Pb, Zn, Ag, Mn and Mo) are combined in Figure 8, enabling comparison. Among these elements, As and Pb concentrations in pyrite are obviously higher than other trace elements, ranging up to 10,428.27 and 4894.31 ppm, respectively. Cobalt and Ni are two important trace elements in pyrite, showing moderate levels of enrichment in this study with highly variable concentrations (0.002~1898.84 and 0.01~511.43 ppm, respectively). While Cu, Ag and Sb are present at measurable levels in pyrite, the contents of Zn, Se, Sn and Mn are relatively lower than those of the trace elements mentioned above (Table S1). However, the average contents of Au (0.17 ppm), Cd (1.63 ppm), V (0.38 ppm), Mo (0.82 ppm), Bi (4.16 ppm) and W (0.43 ppm) of all pyrite samples are very low or below the detection limit, with maximum concentrations of several dozen ppm (Table S1).

**Table 1.** LA-ICP-MS analysis results (in ppm) in different pyrite types of the Xitieshan deposit.

Type	Mn	Co	Ni	Cu	Zn	As	Ag	Sb	Pb
Py0 ( <i>n</i> = 18)									
Min	0.7	3.4	3.2	7.6	1.4	0.3	2.0	0.1	7.7
Max	2369.3	110.6	511.4	1402.8	5729.6	1324.2	747.9	349.4	4894.3
GM	13.7	26.0	39.3	162.6	9.9	6.2	50.2	3.8	478.5
MD	11.4	38.0	100.5	247.4	6.6	4.3	71.3	9.8	883.2
Py1a ( <i>n</i> = 16)									
Min	0.1	0.1	0.2	0.2	0.4	0.2	0.1	0.1	0.1
Max	168.0	1.6	5.2	180.3	3.1	7.4	68.1	189.5	865.5
GM	1.4	0.5	1.4	5.8	1.1	2.0	3.5	3.5	14.3
MD	0.7	0.8	2.4	6.1	1.0	3.8	9.5	6.6	77.8
Py1b ( <i>n</i> = 11)									
Min	0.2	0.1	0.2	0.1	0.7	0.4	0.1	0.5	0.9
Max	17.5	5.3	43.8	1.9	2.9	59.0	2.7	61.0	61.4
GM	1.8	0.5	4.4	0.4	1.5	4.8	0.4	3.8	11.9
MD	1.4	0.4	8.0	0.4	1.8	7.4	0.5	1.9	17.1
Py2a ( <i>n</i> = 17)									
Min	0.1	0.1	0.1	0.1	0.4	57.2	0.1	0.1	0.1
Max	1.7	3.8	3.0	30.7	2.4	10428.3	15.4	145.1	2493.6
GM	0.5	0.3	0.8	0.7	1.4	1740.1	1.4	2.8	1.4
MD	0.6	0.2	1.0	0.5	1.5	2118.2	4.8	2.8	0.4
Py2b ( <i>n</i> = 15)									
Min	0.2	1.3	1.9	0.1	0.6	0.3	0.1	0.1	0.2
Max	10.5	1898.8	179.6	9.8	6.5	1350.9	1.1	28.9	263.5
GM	0.6	60.1	31.9	0.9	1.4	17.1	0.2	1.0	5.0
MD	0.3	60.1	61.4	0.8	1.4	19.2	0.3	0.9	2.9
Py3 ( <i>n</i> = 13)									
Min	0.1	4.0	0.2	0.1	0.4	0.3	0.1	0.1	0.2
Max	194.9	52.1	7.7	7.2	4.2	1.0	1.4	5.3	119.8
GM	1.0	9.7	1.4	0.8	1.2	0.5	0.4	0.6	3.5
MD	0.5	8.9	1.5	1.0	1.3	0.5	0.6	1.2	1.9

Note: Min = minimum, Max = maximum, GM = geometric mean, MD = median. The whole dataset is listed in Table S1 in the Supplementary Materials.

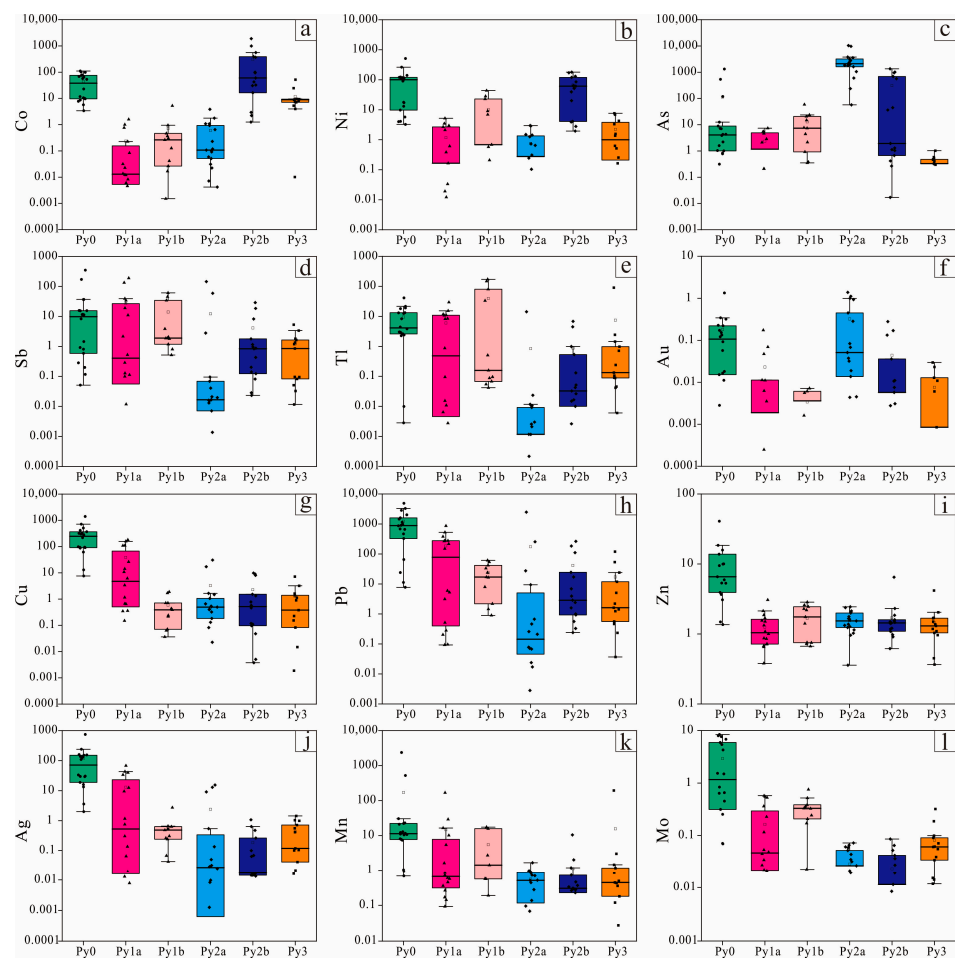


**Figure 8.** Statistical representation of the different types of pyrite in the Xitieshan deposit analyzed via LA-ICP-MS. Concentrations of (a) Co, (b) Ni, (c) As, (d) Sb, (e) Tl, (f) Au, (g) Cu, (h) Pb, (i) Zn, (j) Ag, (k) Mn, and (l) Mo elements of pyrite from different generations. Boxes outline the 25th to 75th percentiles and whiskers extend to the minimum and maximum values. The short line in the box represents the median value, whereas the square without filling represents the mean value.

The colloform pyrite (Py0) exhibits the highest contents of Cu, Pb, Zn, Ag, Mn and Mo and significant contents of Au, Sb and Tl (Figure 8). While the fine-grained anhedral spongy pyrite (Py1) contains relatively high contents of Mn, Mo, Ag, Sb, Cu, Pb and Tl, it is depleted in Co compared with other pyrite varieties (Figure 8). Py0 and Py1 display similar Mn, Sb and Tl concentrations, which are both higher than those of Py2 and Py3. The coarse-grained euhedral pyrite (Py2) has considerably high As and Au contents. There are significant differences in trace element composition between Py1 and Py2, including higher Cu, Ag, Mn, Mo, Pb, Sb and Tl compositions, but lower Co, Ni, As and Au contents, for the Py1 group analyzed. A slight enrichment of Se in Py2 compared to other pyrite groups is recognized (Table S1). Nevertheless, the later veined pyrite (Py3) has observably low concentrations of most elements (Figure 8). The exception to this is Co, which is remarkably enriched in Py3 compared with Py1. Additionally, Mo and Tl are slightly enriched in comparison with Py2. Py2 and Py3 show analogous concentrations of Cu, Pb, Zn and Mn, and both display lower values than those of Py0 and Py1.

## 5.2. Sulfur Isotope Compositions of Sulfides

There were 94 sulfide spots analyzed to obtain the sulfur isotopic compositions of the Xitieshan deposit, consisting of 32 spots on sulfides from stratiform or massive ores in schist, 43 spots on sulfides from stockwork ores in marble, schist and discolored rocks, and 19 spots on sulfides from veined ores in Formation C siltstones. The complete analyzed

dataset is provided in Supplementary Table S2. The sulfur isotopes in sulfides from different parts of submarine hydrothermal systems show significant change, moving from relatively narrow values ( $-5.3\text{‰}$ – $5.6\text{‰}$ ) in stratiform or massive orebodies in schist, with an average value of  $2.6\text{‰}$ , to prominently positive and variable values ranging from  $-1.7\text{‰}$  to  $32.0\text{‰}$  in stockwork ores taken from marble, schist and strongly discolored alteration rocks (mean of  $10.4\text{‰}$ ) (Figure 9). Conversely, the veined sulfides in Formation C siltstones display near-zero  $\delta^{34}\text{S}$  values varying between  $0.6\text{‰}$  and  $4.5\text{‰}$  with an average of  $2.8\text{‰}$ , spanning a range narrower of values than ores in schist, marble or discolored rocks. In conclusion, sulfides from different types of mineralization feature distinct S isotopic compositions.

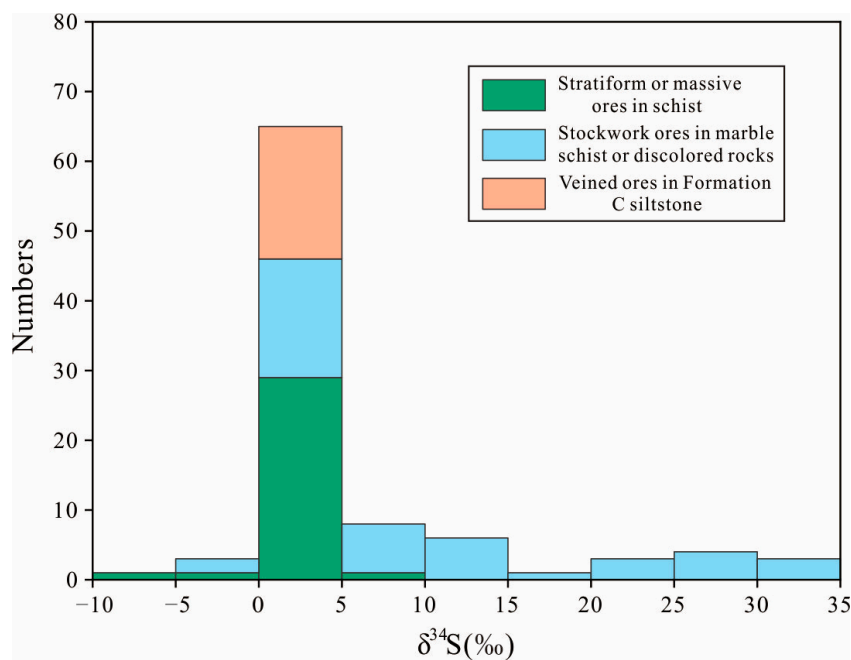


**Figure 9.** Sulfur isotope histogram for the sulfides from different mineralization types in the Xitieshan deposit.

## 6. Discussion

### 6.1. Occurrences of Trace Elements in Pyrite

Pyrite is among the most common sulfides in submarine hydrothermal deposits. Its trace element composition has been widely studied, constituting a large mineral chemical dataset [52,53]. In general, there are significant concentrations of As, Au, Co, Ni, Cu, Pb, Zn, Ag, Se, Sb, Te, Tl, Bi and Hg in pyrite [54,55]. Trace element occurrences in pyrite likely follow several modes [56]: (1) visible micron-sized sulfide inclusions, (2) visible micron-sized oxides or silicate inclusions, (3) invisible sulfide nanoparticles, and (4) invisible solid solutions within the crystal lattice. LA-ICP-MS time-resolved profiles can provide straightforward information about trace element distributions in pyrite. Figure 10 illustrates typical time-resolved LA-ICP-MS signals for pyrite in the Xitieshan deposit. The majority of ablation profiles examined in this study display smooth patterns for Fe, Co, Ni, Se, Sb, Sn and Mo (Figure 10a), implying their occurrence as primarily structural substitutes or nano-inclusions. As the most common non-stoichiometric replacement in pyrite, they are generally substitutes for S [57]. However, the difference of valence for S and As ions leads to the imbalance of charge and requires the incorporation of trivalent cations such as  $\text{Sb}^{3+}$  to retain the charge balance [58], as suggested by the distinctly positive correlation between Sb and As of most pyrite samples in this study (Figure 11a). Conversely, Py2 are distributed outside the correlation trend, and a prominent positive association between Pb and As for a large proportion of pyrite subpoints can still be observed, with the exception of Py2 (Figure 11b). Both facts likely result from the anomalous enrichment of As in recrystallized Py2. In the Xitieshan deposit, the contents of Au covariant moderately with those of As,

with almost all the pyrite samples plotted below the gold saturation line (Figure 11c), indicating that Au basically possesses a lattice-bound distribution in pyrite with a coupled substitution of  $\text{As}^{3+}$  and  $\text{Au}^+$  for  $2\text{Fe}^{2+}$  [59]. With the exception of Au, Ag is also generally elevated in pyrite when associated with As analyses [60]. In the log As vs. log Ag diagram (Figure 11d), a great number of sample points are located in the triangular wedge-shaped area (gray dashed lines), which is interpreted to reflect lattice substitution [55]. Conversely, most Py0 samples with higher Ag contents are situated above the triangular wedge-shaped field in the Ag-As diagram, possibly suggesting the existence of Ag-mineral inclusions certified by the irregular ablation profile for Ag in colloform pyrite (Figure 10b).

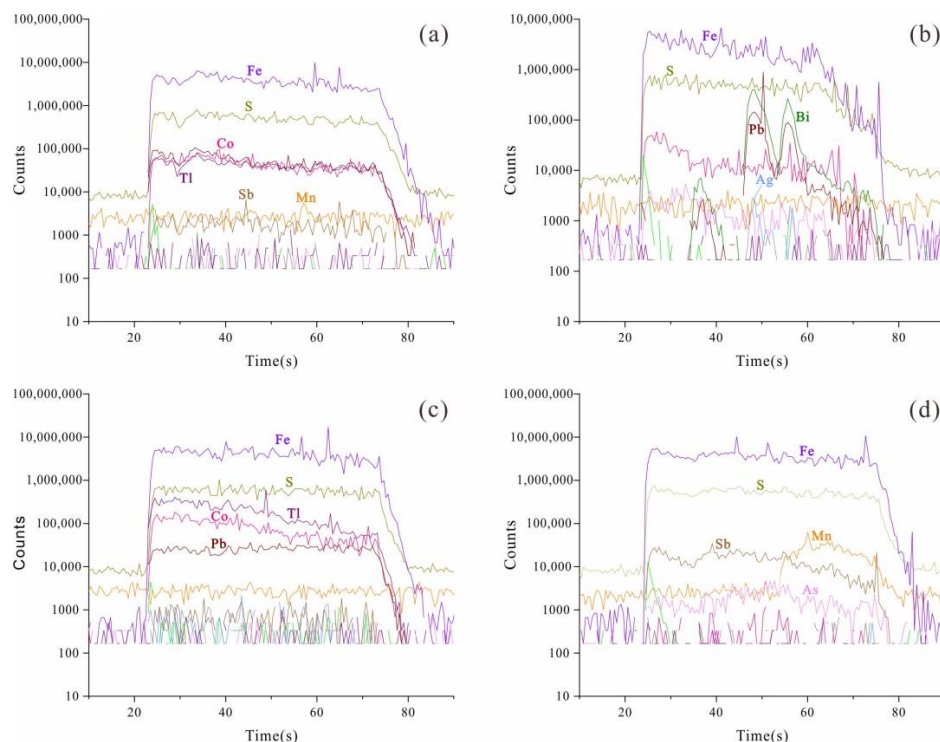


**Figure 10.** Examples of LA-ICP-MS profiles (time-resolved) for pyrite from the Xitieshan deposit. (a) Ablation profile for pyrite showing smooth traces for Fe, Co, Ni, Se, Sb, Sn and Mo; (b) ablation profile for colloform pyrite showing galena (Pb-Bi-Ag) inclusion; (c) ablation profile for euhedral pyrite showing smooth traces for Pb, likely present as lattice substitutions; (d) ablation profile for pyrite showing Mn-rich inclusion.

The metallogenic elements in the Xitieshan pyrites are dominated by Pb and Zn, with secondary elements of Au and Ag, and lesser Cu. Pb cannot enter the crystal lattice of pyrite readily as a result of its larger ionic size compared with Fe and its high rates of water exchange [61], which is further reflected by the irregular ablation profiles for Pb in colloform pyrite from the Xitieshan deposit (Figure 10b). The overall parallel ablation signal curves of Bi and Pb, combined with their roughly positive correlations (Figure 11e), demonstrate that Bi measured in pyrite is mainly hosted in galena inclusions, especially in colloform pyrite. On the contrary, the observation of a smooth depth profile for Pb in Py2 (Figure 10c) presumably reflects its use as a lattice replacement (or nano-inclusions) rather than as micro-inclusions. A perfect positive Spearman rank correlation between Cu and Ag was identified in this study (Figure 11f), which is possibly associated with the inclusion of chalcopyrite in pyrite [62]. Silver also shows a strong association with Pb (Figure 11g). Irregular ablation profiles for Mn can be locally observed in Xitieshan pyrite (Figure 10d), indicating the occurrence of Mn-carbonate or Mn-oxide inclusions. Additionally, vanadium is moderately positively correlated with Mn (Figure 11h), which is likely a result of seawater mixing during the formation of Xitieshan pyrite.

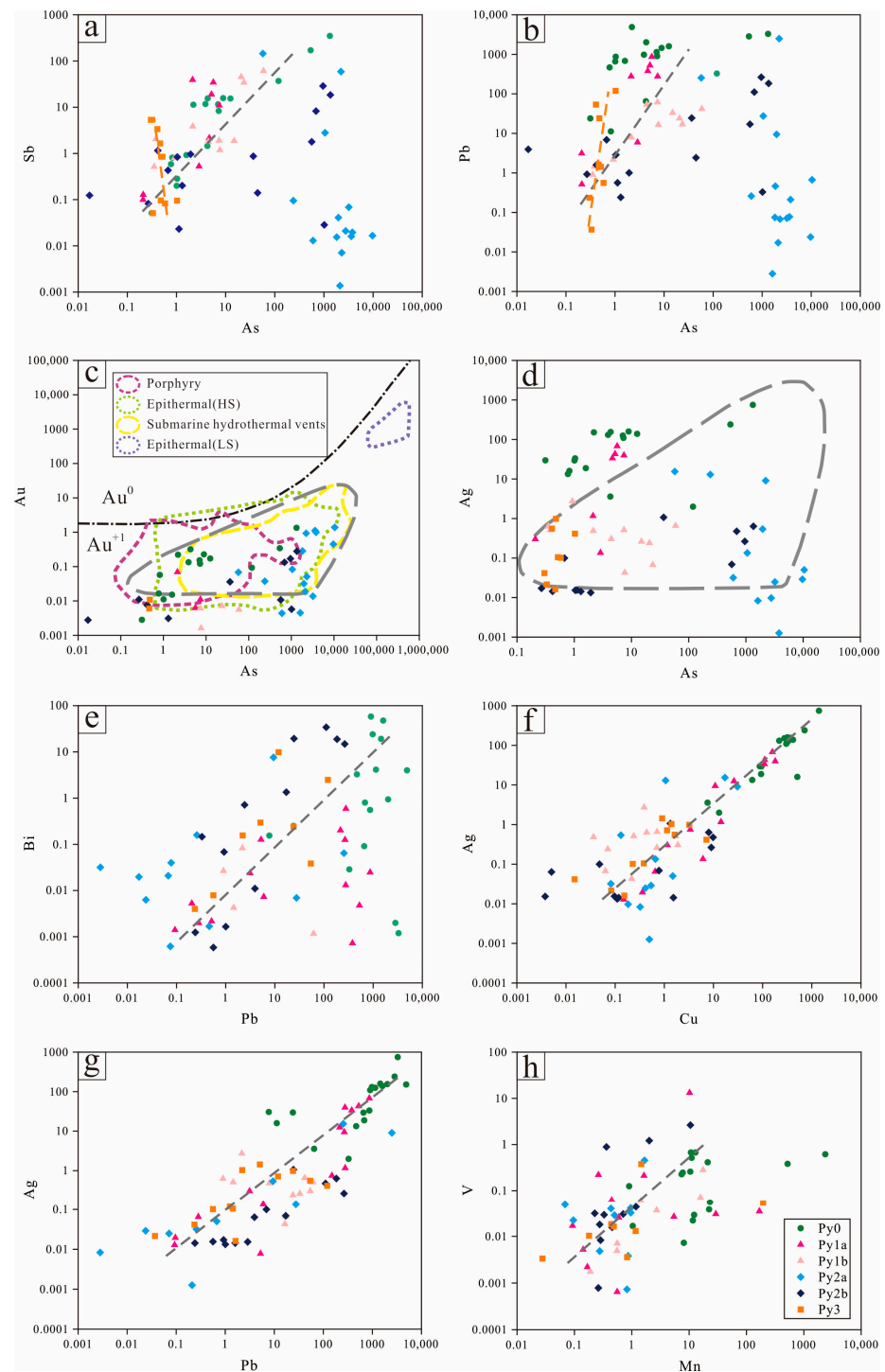


**Figure 11.** Binary plots of (a) As vs. Sb, (b) As vs. Pb, (c) As vs. Au, (d) As vs. Ag, (e) Pb vs. Bi, (f) Cu vs. Ag, (g) Pb vs. Ag, and (h) Mn vs. V trace elements in the four-type pyrites of the Xitieshan deposit. The pyrite fields for Epithermal (HS and LS) and Porphyry deposits are from [63] and references therein. The field for pyrite in submarine hydrothermal vents is from [52]. The black dashed curve of the Au solubility line represents the upper limit of the Au solid solution in pyrite as a function of As [57]. The gray dashed line defines the wedge-shaped zone indicating the trace element solid solution of Au and Ag for pyrites that plot within this stage [52,55,57,60]. The gray dashed straight line represents a linear relationship composed of most pyrite data points, while the orange dashed straight line in (a) and (b) represents a minor distinct linear relationship composed of Py3 data points.

## 6.2. Pyrite Genesis

Detailed petrographic studies of pyrite from the Xitieshan deposit provided an opportunity to classify the different types of material. In this study, initial pyrite emerges primarily as preserved colloform pyrite or weakly affected fine-grained anhedral spongy pyrite (Figure 7a,b), which are similar to the pyrite from massive sulfide deposits such as the Rammelsberg, Red Dog and Caribou deposits and black smoker systems on the modern seafloor [52,64–66], displaying submarine hydrothermal mineralization features. Py1 is distinguished by numerous larger pore spaces that are mainly filled with silicate minerals (Figure 7f), probably indicative of coeval crystallization, with these phases resulting from weak recrystallization during the initial stage of orogeny. Nevertheless, the laminar-like Py2 aggregates, which are more euhedral than the bedded spongy Py1a, were likely formed by further recrystallization of the latter (Figure 7h). Moreover, the Py2 grain size was unusually large in some ores (Figure 7i), suggesting extensive recrystallization and overgrowth of primitive pyrite due to higher-grade metamorphism, where pyrite crystal with a larger diameter is usually associated with stronger deformation [67]. The typical core–rim texture of pyrite (Figure 7j) indicates increased degrees of the recrystallization of generations where Py2 overprinted Py1. The rounded Py2 grains with curved boundaries distributed in the pyrrhotite matrix were also found in typical massive ore facies, suggesting equilibrium annealing during the process of deformation [68]. On the other hand, the contact relationships of Py3 between Silurian Formation C siltstones (Figure 7q) and early-formed sulfides (Figure 7r,s) manifest as a product of overprinted hydrothermal activities. In other words, colloform pyrite is usually surrounded by anhedral–subhedral spongy pyrite, and both are replaced by the later pyrite vein (Figure 7r), reflecting multiple phases of pyrite precipitations that probably correspond with different mineralized events.

The geochemical composition systematics of pyrite are sensitive to subtle changes in temperature and composition of the hydrothermal system from which it was precipitated, which can be employed to trace variations in fluid properties with the evolution of the mineralization, evaluate the genesis of ore deposits, and even provide guidance for mine exploration [55,69–71]. The prominent trace element variation in different generations of pyrite in the Xitieshan deposit can be used to constrain the origin and fluid- and precipitation-related processes, being a proxy for tracing the complete mineralized process involving different metallogenic events. Au is comparatively enriched in colloform pyrite (Py0) because it can precipitate in the minute pores or interstitial spaces of syn-sedimentary colloform grains [61]. Additionally, the relatively higher Bi content of Py0 with a mean value >1 ppm indicates that they are likely influenced by sediments. Moreover, the absorbability on the surface of colloform and fine-grained spongy pyrites is strong during the aggregation of pyrite crystals [72], leading to high Mn contents in Py0 and Py1 (Figure 8k). The growth of these minute pyrite crystals combined with the incorporation of subcolloidal and colloidal particles can result in compatibility of trace elements such as Tl [73]. In this study, the colloform and fine-grained spongy pyrite show high Tl concentrations with average values of 9.52 and 22.11 ppm (Figure 8e), suggesting a syngenetic origin.

On the other hand, Py2 of tectonic fabric is obviously discordant with Py0 and Py1 due to its euhedral shape, clean surface and larger grain size, becoming idiomorphic and coarser-grained in relation to colloidal and porous pyrite upon recrystallization. During the process of deformation, both the modification of texture and the remobilization of pyrite occurred, accompanied by variation in trace element compositions and featuring markedly decreasing concentrations of Cu, Pb, Zn, Ag, Mo and Mn from Py0 to Py2 (Figure 8) along with the enhancement of metamorphism, indicating the expulsion of most elements during zone refining. Previous studies have shown that metamorphism can lead to the release and subsequent mobilization of elements such as Cu, Pb, Zn and Mo, appearing as nano-inclusions or non-stoichiometric substitutions in the original pyrite, and subsequently precipitate them into codependent minerals or into new phases, resulting in low trace element contents in recrystallized pyrite [58]. This is suggested by the irregular ablation profiles of colloform pyrite for Pb, the occurrence of Ag as an inclusion, and

the contrast smooth LA-ICP-MS time-resolved signal of recrystallized pyrite (Figure 10), combined with the losses of these elements present in inclusions. The metamorphic hydrothermal fluid-leached trace elements from the initial pyrite are accompanied by the nearly simultaneous precipitation of the later-stage Cu-, Pb-, Zn- and Sb-bearing sulfide minerals [69,74]. In the Xitianshan deposit, the Pb and Zn contents greatly decreased from Py0 to Py2 due to metamorphism. This contributed to the formation of the dominating later-stage sphalerite and galena [58]. These results are consistent with the conclusions of previous studies [25], further indicating the significance of metamorphism for mineralization enrichment. This was further reflected by the phenomenon whereby Py0 and Py1 were replaced by porous sphalerite (Figure 7f), suggesting a formation before the latter, while Py2 usually displayed jagged boundaries with homogeneous sphalerite (Figure 7n), implying that Sp2 was formed after metamorphic pyrite. However, some other trace elements, e.g., As, Co, Ni and Se, occurring as stoichiometric replacement in pyrite, displayed roughly consistent or higher contents than Py1 to Py2 in this study (Figure 8; Table S1), implying that metamorphism could also lead to enrichment in trace elements that remain in the solid solution [56,67,69,75]. The significant positive correlation between As and Au in this study reflects the incorporation of these elements from the metamorphic fluids. In other words, metamorphic recrystallization played an important role in controlling the further Pb-Zn enrichment in the Xitianshan deposit.

The Co, Ni contents and Co/Ni ratios of pyrite are normally used as indicators to distinguish the physicochemical formation conditions [67,74,76]. Generally, low Co/Ni ratios below 1 are described as representing syn-sedimentary pyrite [61,75], while highly variable Co/Ni ratios greater than those for pyrite are thought to be the result of magmatic-hydrothermal processes [77]. In this study, Py0 contains variable Co and Ni contents with a relatively narrow extent of Co/Ni ratios from 0.19 to 2.96 (average 0.92), and the majority of the spots are located below the Co/Ni = 1 line (Figure 12a), demonstrating syn-sedimentary affinities. Conversely, the Co/Ni ratios of Py3 range from 2.22 to 54.46 (average 13.80), resembling typical magmatic-hydrothermal pyrite. Moreover, the Py0 samples with relatively higher Zn and Pb concentrations fall near the boundaries of the diagenetic pyrite and hydrothermal pyrite fields in the Zn vs. Pb discrimination diagram (Figure 12b), indicating a submarine exhalation origin that shows both the sedimentary and hydrothermal properties. The Zn and Pb contents of Py3 samples are comparatively lower, being mainly plotted in the field of hydrothermal pyrite, further reflecting an association with magmatic hydrothermal activity. The comparatively low concentrations of most elements in Py3 are possibly ascribed to the infertilities of the hydrothermal fluid itself.

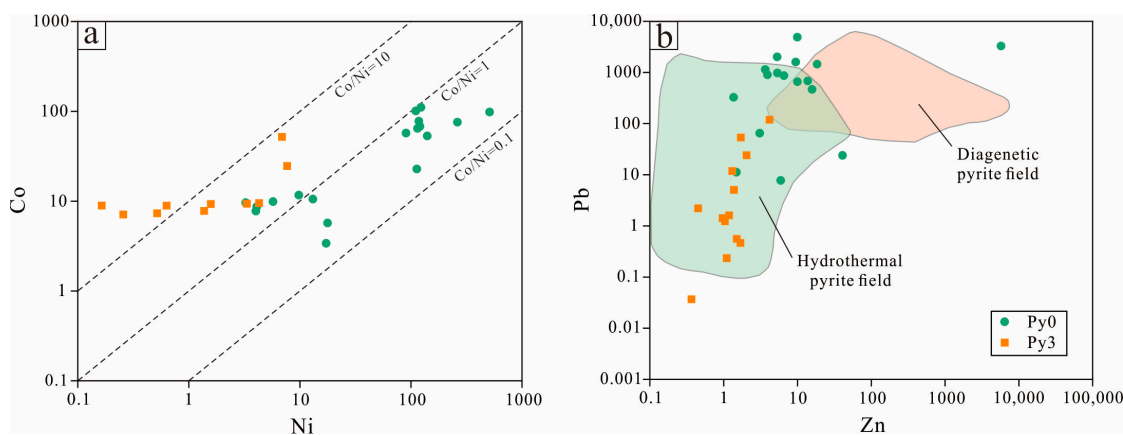


**Figure 12.** (a) Co vs. Ni; (b) Pb vs. Zn diagrams for the Xitianshan colloform (Py0) and later veined (Py3) pyrites.

### 6.3. Source of Sulfur

Different types of massive sulfide deposits such as SEDEX, VMS and VSHMS usually display distinct sulfur isotopic compositions. The  $\delta^{34}\text{S}$  values of SEDEX deposits are generally about 15‰ lower than those of contemporaneous seawater, which instead have wide variations [78], showing the features of thermochemical or biological reductions of seawater sulfate. However, the sulfur isotope ranges of sulfides in VMS deposits are usually narrower than those in SEDEX deposits, with S isotopic compositions being close to zero or relatively positive, exhibiting the characteristics of magmatic sulfur or sulfate thermochemical reduction, in which magmatic sulfur can be derived from the leaching of underlying volcanic rocks by circulating hydrothermal fluid or directly via magmatic gas release [79,80]. On the other hand, previous S isotope studies have been carried out on deposits of the Iberian Pyrite Belt, Bathurst Mining Camp and Finlayson Lake District (Wolverine) [81–84]. These are considered a transitional type named VSHMS deposit, which occurs between typical VMS and SEDEX deposits [84–87]. The studies showed that  $\delta^{34}\text{S}$  values in the sulfides of these deposits are roughly positive with minor negative values. Values vary significantly between distinct zones of the submarine hydrothermal system, with upward increases in average  $\delta^{34}\text{S}$  values from 14.2‰ in bedded ore to 15.8‰ and 16.1‰ in vent complex and underlying stringer ores, respectively, of the Brunswick No. 12 deposit [81]. Additionally,  $\delta^{34}\text{S}$  values ranged from  $-8\%$  to  $-2\%$  in syngenetic sulfides and from  $+3\%$  to  $+5\%$  in stockwork sulfides [82], and mean  $\delta^{34}\text{S}$  values ranged from 0.8‰ in massive sulfide lens minerals to 12.0‰ in sulfide stringer veins of the Wolverine deposit [84]. In other words, the  $\delta^{34}\text{S}$  values of sulfides in these deposits display systematic variations between different mineralized parts, which are consistently more positive in lower stringer or stockwork units than in upper massive or laminated units. The sulfur isotope compositions of the Xitieshan deposit are similar to those of VSHMS deposits with  $\delta^{34}\text{S}$  values zoned stratigraphically upward, moving from the stratiform or massive sulfides in schist to stockwork sulfides (Figure 9). Namely, the stringer or stockwork sulfides in marble, schist or discolored rocks are generally isotopically heavier ( $\delta^{34}\text{S} = -1.7\%$ ~ $32.0\%$ ) than contemporaneous bedded or massive sulfides in schist ( $\delta^{34}\text{S} = -5.3\%$ ~ $5.6\%$ ), with mean value of 10.4‰ and 2.6‰, respectively (Table S2). On the other hand, compared with the previous sulfur isotopic data of sulfides in the Xitieshan deposit featuring a relatively narrow range (2.08‰~5.81‰) [25], the S isotopic compositions in this paper are characterized by obviously more positive values and a broader range based on more comprehensive analysis of different types of ore samples, probably reflecting different sources of sulfur or different sulfate reduction mechanisms.

The initial formation of the Xitieshan deposit was presumably associated with the circulation flow of heated seawater in a convective system, showing the obvious differences in S isotope compositions in sulfide between the massive and stringer zones, which generally occurred due to the distinct mode of sulfate reduction. Of these, the apparent positive  $\delta^{34}\text{S}$  values of the stringer sulfides in marble, schist and discolored rocks may reflect the inorganic reduction of seawater sulfate, possibly achieved via reaction with  $\text{Fe}^{2+}$  under relatively high-temperature hydrothermal conditions [88], whose huge variations are probably attributable to the distinct degrees of reduction that governs the  $\text{SO}_4\text{:H}_2\text{S}$  ratio [89]. This feature contrasts with the lamellar or massive sulfides in schist that generally exhibit a relatively narrow range of  $\delta^{34}\text{S}$  values ( $-5.3\%$ ~ $5.6\%$ ), probably indicating a relatively homogeneous bacterial reduction from  $\text{SO}_4^{2-}$  under similar closed or partly closed conditions in an ambient anoxic water column [82,83]. Organic materials have been widely observed stratigraphically in the Xitieshan deposit, including carbonaceous schist. Of course, more evidence of fluid inclusion is needed to prove the different reduction modes (TSR and BSR) of the different styles of sulfides in this study. On the whole, the sulfur isotope features of the Xitieshan deposit are similar to the typical VSHMS deposits, especially the Wolverine deposit (Figure 13), showing distinct  $\delta^{34}\text{S}$  compositions of the different submarine hydrothermal zones, probably related to a change in the mode of reduction, which was likely controlled by local geological environments. However, the veined sulfides in Formation C

siltstone show S isotopic compositions mostly close to 0‰, with  $\delta^{34}\text{S}$  values ranging from 0.6‰ to 4.5‰. This is consistent with typical magmatic–hydrothermal sulfur features [77]. Hence, we concluded that the formation of this mineralization type was associated with minor post-orogenic superimposed magmatic–hydrothermal activity.

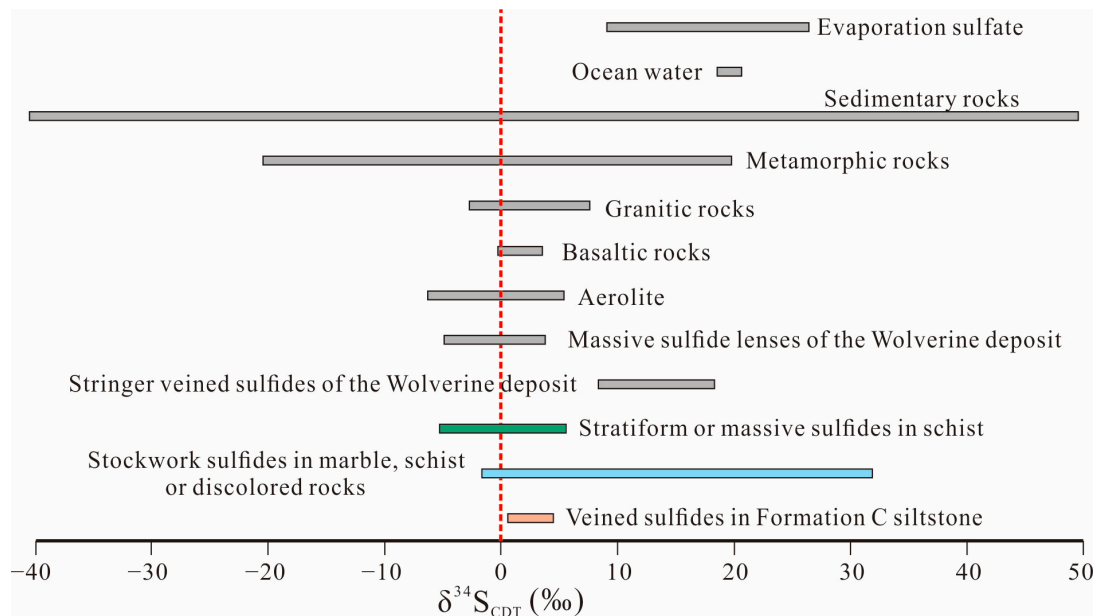


**Figure 13.** Sulfur isotope composition diagram for sulfides from different mineralization types in the Xitianshan deposit.  $\delta^{34}\text{S}$  data of the Wolverine deposit is from [84].

## 7. Conclusions

(1) The  $\delta^{34}\text{S}$  values of sulfides in stockwork ores and massive laminar ores range from  $-1.7\text{‰}$  to  $+32\text{‰}$  and  $-5.3\text{‰}$  to  $+5.6\text{‰}$ , probably indicating that sulfur is derived from the thermochemical and biological reduction of seawater sulfates, respectively, which is similar to the case of typical VSHMS deposits.

(2) Orogenic metamorphism leads to the release and subsequent mobilization of elements such as Cu, Pb, Zn, Ag, Mo, Mn and Sn, appearing as inclusions in the initial colloform and anhedral spongy pyrites, and subsequently precipitates them into new sulfide phases, which is critical to the further Pb–Zn enrichment of the Xitianshan deposit.

(3) There is a minor post-orogenic magmatic hydrothermal event superimposed in the Xitianshan deposit.

**Supplementary Materials:** The following supporting information can be downloaded at: <https://www.mdpi.com/article/10.3390/min13121549/s1>, Table S1: LA-ICP-MS trace element data (ppm) of different types of pyrite from the Xitianshan deposit; Table S2: Sulfur isotopic compositions of sulfides from different types of mineralization in the Xitianshan deposit.

**Author Contributions:** Conceptualization, H.Y. and H.S.; field investigation, H.Y. and H.S.; experiments, H.Y.; data curation, H.Y.; writing—original draft preparation, H.Y.; writing—review and editing, H.Y. and H.S. All authors have read and agreed to the published version of the manuscript.

**Funding:** This research was funded by the National Natural Science Foundation of China and West Mining Corporation (China), grant number 41172087 and 41502067.

**Data Availability Statement:** Data are contained within the article and supplementary materials.

**Acknowledgments:** We are grateful to Zhixing Feng, Yongsheng Zhong and Li Sun for their help in field investigation and sampling. We also thank Qianrong Fan, Dongsheng Zhu and RuYi Wang for their help with sample preparation and handling.

**Conflicts of Interest:** The authors declare no conflict of interest.

## References

1. Leach, D.L.; Sangster, D.F.; Kelley, K.D.; Large, R.R.; Garven, G.; Allen, C.R.; Gutzmer, J.; Walters, S. Sediment-Hosted Lead-Zinc Deposits: A Global Perspective. In *Economic Geology 100th Anniversary Volume*; Society of Economic Geologists: Littleton, CO, USA, 2005; pp. 561–607.
2. Mills, H.K.; Piercey, S.J.; Toole, T. Geology, alteration, and lithogeochemistry of the Hood volcanogenic massive sulfide (VMS) deposits, Nunavut, Canada. *Miner. Deposita* **2016**, *51*, 533–556. [[CrossRef](#)]
3. Chapman, L.H. Geology and Mineralization Styles of the George Fisher Zn-Pb-Ag Deposit, Mount Isa, Australia. *Econ. Geol.* **2004**, *99*, 233–255. [[CrossRef](#)]
4. Franklin, J.M.; Gibson, H.L.; Jonasson, I.R.; Galley, A.G. Volcanogenic massive sulfide deposit. In *Economic Geology 100th Anniversary Volume*; Society of Economic Geologists: Littleton, CO, USA, 2005; pp. 523–560.
5. Allen, R.L.; Weihed, P. Global comparisons of volcanic-associated massive sulphide districts. *Geol. Soc. Spec. Publ.* **2002**, *204*, 13–37. [[CrossRef](#)]
6. Sun, C.; Yang, X.Y.; Zhang, H.S.; Ji, W.H.; Chen, B.; Dong, Z.C.; Faisal, M.; Xi, D.H. Tracing the formation and modification of the Keketale VMS-type Pb-Zn deposit, Altai Mountains: Insights from ore deposit geology, geochronology, and magnetite geochemistry. *Ore Geol. Rev.* **2022**, *144*, 104852. [[CrossRef](#)]
7. Bailie, R.H.; Reid, D.L. Ore textures and possible sulphide partial melting at Broken Hill, Aggeneys, South Africa I: Petrography. *S. Afr. J. Geol.* **2005**, *108*, 51–70. [[CrossRef](#)]
8. Gu, L.X.; Zheng, Y.C.; Tang, X.Q.; Fernando, D.; Wu, C.Z.; Tian, Z.M.; Lu, J.J.; Ni, P.; Li, X.; Yang, F.T. Copper, gold and silver enrichment in ore mylonites within massive sulphide orebodies at Hongtoushan, NE China. *Ore Geol. Rev.* **2007**, *30*, 1–29. [[CrossRef](#)]
9. Vikentyev, I.V.; Belogub, E.V.; Novoselov, K.A.; Moloshag, V.P. Metamorphism of volcanogenic massive sulphide deposits in the Urals. Ore geology. *Ore Geol. Rev.* **2017**, *85*, 30–63. [[CrossRef](#)]
10. Agnew, M.W.; Large, R.R.; Bull, S.W. Lewis Ponds, a hybrid carbonate and volcanic-hosted polymetallic massive sulphide deposit, New South Wales, Australia. *Miner. Deposita* **2005**, *39*, 822–844. [[CrossRef](#)]
11. Zheng, Y.; Zhang, L.; Chen, Y.J.; Hollings, P.; Chen, H.Y. Metamorphosed Pb–Zn–(Ag) ores of the Keketale VMS deposit, NW China: Evidence from ore textures, fluid inclusions, geochronology and pyrite compositions. *Ore Geol. Rev.* **2013**, *54*, 167–180. [[CrossRef](#)]
12. Zhong, R.C.; Li, W.B. The multistage genesis of the giant Dongshengmiao Zn-Pb-Cu deposit in western Inner Mongolia, China: Syngenetic stratabound mineralization and metamorphic remobilization. *Geosci. Front.* **2016**, *7*, 529–542. [[CrossRef](#)]
13. Wang, D.; Zheng, Y.Y.; Mathur, R.; Jiang, J.S.; Zhang, S.K.; Zhang, J.F.; Yu, M. Multiple mineralization events in the Zhaxikang Sb–Pb–Zn–Ag deposit and their relationship with the geodynamic evolution in the North Himalayan Metallogenic Belt, South Tibet. *Ore Geol. Rev.* **2019**, *105*, 201–215. [[CrossRef](#)]
14. Fu, J.G.; Liang, X.Q.; Wang, C.; Zhou, Y.; Jiang, Y.; Dong, C.G. The Xitieshan volcanic sediment-hosted massive sulfide deposit, North Qaidam, China: Geology, structural deformation and geochronology. *Ore Geol. Rev.* **2017**, *80*, 923–946. [[CrossRef](#)]
15. Wu, G.B.; Sun, H.S.; Feng, Z.X.; Fan, J.C.; Lu, J.P.; Wang, Y.Q. The paleotectonic setting of Xitieshan lead–zinc deposit. *Geochimica* **2010**, *39*, 229–239. (In Chinese with English Abstract)
16. Sun, H.S.; Zhao, L.J.; Wu, G.B.; Ning, J.T.; Chen, Q.M.; Jiang, C.L. Metallogenic tectonic setting and ore-finding potential of Xitieshan massive sulfide lead–zinc deposit: Evidence from lithochemistry and geochemistry of ore-hosted volcanic strata, Tanjianshan Group. *Acta Petrol. Sin.* **2012**, *28*, 652–664. (In Chinese with English Abstract)
17. Sun, H.S.; Li, H.; Evans, N.J.; Yang, H.; Wu, P. Volcanism, mineralization and metamorphism at the Xitieshan Pb–Zn deposit, NW China: Insights from zircon geochronology and geochemistry. *Ore Geol. Rev.* **2017**, *88*, 289–303. [[CrossRef](#)]
18. Song, S.G.; Niu, Y.L.; Su, L.; Xia, X.H. Tectonics of the North Qilian orogeny, NW China. *Gondwana Res.* **2013**, *23*, 1378–1401. [[CrossRef](#)]
19. Sun, H.S.; Li, H.; Algeo, T.J.; Gabo-Ratio, J.A.S.; Yang, H.; Wu, J.H.; Wu, P. Geochronology and geochemistry of volcanic rocks from the Tanjianshan Group, NW China: Implications for the early Paleozoic tectonic evolution of the North Qaidam Orogen. *Geol. J.* **2018**, *54*, 1769–1796. [[CrossRef](#)]
20. Zhu, X.Y.; Deng, J.N.; Wang, J.B.; Lin, L.J.; Fan, J.C. The exhalation-sedimentary system of Xitieshan lead-zinc deposit, Qinghai Province. *Geol. Prospect.* **2006**, *42*, 18–23. (In Chinese with English Abstract)
21. Zhu, X.Y.; Deng, J.N.; Wang, J.B.; Lin, L.J.; Fan, J.C.; Sun, S.Q. Identification and study of stockwork altered pipe of Xitieshan lead-zinc deposit, Qinghai Province. *Geochemistry* **2007**, *36*, 37–48. (In Chinese with English Abstract)
22. Zhu, X.Y.; Wang, L.J.; Zhu, G.C.; Deng, J.N.; Fan, J.C. Characteristics of sulfur isotope geochemistry of Xitieshan lead-zinc deposit, Qinghai: The mixing of sulfurs from hydrothermal and seawater. *Acta Petrol. Sin.* **2010**, *26*, 657–666. (In Chinese with English Abstract)
23. Jian, R.T.; Li, F.; Zhao, X.D. Rare earth element geochemistry of the Xitieshan carbonaceous schist type Pb-Zn deposit, Qinghai Province. *Geol. Explor.* **2009**, *45*, 240–246. (In Chinese with English Abstract)
24. Wu, J.R.; Ren, B.C.; Zhang, M.; Gao, D.C.; Zhao, T.; Zhang, H.W.; Song, Z.G.; Zhang, Q.L. The genetic type and geological characteristics of the Xitieshan massive sulphide deposit, Qinghai. *Bull. Xi'an Inst. Geol. Miner. Resour.* **1987**, *20*, 1–88. (In Chinese with English Abstract)

25. Feng, Z.J.; Yang, T.; Yao, X.Z.; Brzozowski, M.J.; Lei, R.X.; Wu, C.Z. Ore forming and reworking processes in the Xitieshan Pb–Zn deposit, Qinghai Province, China: Constraints from in situ trace-element and S isotope compositions of sulfides. *Ore Geol. Rev.* **2022**, *149*, 105103. [[CrossRef](#)]
26. Feng, Z.X.; Sun, H.S.; Wu, G.B.; Wang, Y.Q. A discussion on type of the Xitieshan Pb–Zn ore deposit, Qinghai. *Geol. Rev.* **2010**, *56*, 501–512. (In Chinese with English Abstract)
27. Zhang, G.B.; Zhang, L.F.; Christy, A.G. From oceanic subduction to continental collision: An overview of HP–UHP metamorphic rocks in the North Qaidam UHP belt, NW China. *Asian J. Earth Sci.* **2013**, *63*, 98–111. [[CrossRef](#)]
28. Wu, C.L.; Gao, Y.H.; Li, Z.L.; Lei, M.; Qin, H.P.; Li, M.Z.; Liu, C.H.; Frost, R.B.; Robinson, P.T.; Wooden, J.L. Zircon SHRIMP U–Pb dating of granites from Dulan and the chronological framework of the North Qaidam UHP belt, NW China. *Sci. China Earth Sci.* **2014**, *57*, 2945–2965. [[CrossRef](#)]
29. Zhao, Z.X.; Wei, J.H.; Santosh, M.; Liang, S.N.; Fu, L.B.; Zhao, S.Q.; Li, H. Late Devonian postcollisional magmatism in the ultrahigh-pressure metamorphic belt, Xitieshan terrane, NW China. *Geol. Soc. Am. Bull.* **2018**, *130*, 999–1016. [[CrossRef](#)]
30. Li, P.; Li, Y.B.; Wang, H.F.; Shi, W.J.; Zhao, Z.X.; Liu, M.H.; Feng, Z.X.; Wei, J.H.; Sun, H.S. Structural Characteristics and Ore-controlling Law of Xitieshan Lead-Zinc Mine in North Qaidam Basin. *Bull. Geol. Sci. Technol.* **2019**, *38*, 108–123. (In Chinese with English Abstract)
31. Wang, H.C.; Lu, S.N.; Yuan, G.B.; Xin, H.T.; Zhang, B.H.; Wang, Q.H.; Tian, Q. Tectonic setting and age of the Tanjianshan Group on the northern margin of the Qaidam basin. *Geol. Bull. China.* **2003**, *22*, 488–493. (In Chinese with English Abstract)
32. Lu, S.N. Major Precambrian Events in Northwestern China. *Gondwana Res.* **2001**, *4*, 692. [[CrossRef](#)]
33. Zhang, D.Q.; She, H.Q.; Feng, C.Y.; Li, D.X.; Li, J.W. Geology, age, and fluid inclusions of the Tanjianshan gold deposit, western China: Two orogenies and two gold mineralizing events. *Ore Geol. Rev.* **2009**, *36*, 250–263.
34. Du, W.; Wu, R.; Xu, R.; Zheng, Y.Y.; Chen, X.; Cai, P.; Lu, R.; Wang, H.; Bai, J.; Fan, X.; et al. Establishment of the prospecting model and geological implication of Shuangkoushan style lead–silver deposit in the northern edge of Qaidam basin. *Miner. Explor.* **2016**, *7*, 914–922. (In Chinese with English Abstract)
35. Wang, H.J.; Zheng, Y.Y.; Xu, R.K. Genesis of the Lvliangshan Copper Deposit in Qinghai Province, New Evidence from Geochemical Characteristics and Sedimentary Environment of Cherts. *Geol. Explor.* **2017**, *53*, 63–77. (In Chinese with English Abstract)
36. Cai, P.J.; Xu, R.K.; Zheng, Y.Y.; Yin, Y.M.; Chen, X.; Fan, X.B.; Ma, C. Fluid Inclusion and H–O–S–Pb Isotope Geochemistry of the Yuka Orogenic Gold Deposit, Northern Qaidam, China. *Geofluids* **2019**, *2*, 6912519. [[CrossRef](#)]
37. Fan, X.B. A Discussion on Genesis of Yuqia Gold Deposit in Da Chaidan of Qinghai Province. Master’s Thesis, China University of Geosciences, Beijing, China, 2017. (In Chinese with English Abstract)
38. Xu, G.D. The Genesis Study of Shuangkoushan Lead-Zinc Deposit, Qinghai Province. Master’s Thesis, China University of Geosciences, Wuhan, China, 2012. (In Chinese with English Abstract)
39. Xin, H.T.; Wang, H.C.; Zhou, S.J. Geological events and tectonic evolution of the north margin of the Qaidam Basin. *Geol. Survey Res.* **2006**, *29*, 311–320. (In Chinese with English Abstract)
40. Zhao, Z.X.; Wei, J.H.; Liang, S.N.; Gao, T. Sulfide remobilization and trace element redistribution during metamorphism and deformation at the Xitieshan Pb–Zn deposit, NW China. *Ore Geol. Rev.* **2021**, *136*, 104170. [[CrossRef](#)]
41. Zhao, F.Q.; Guo, J.J.; Li, H.K. Geological characteristics and isotopic age of Tanjianshan Group along northern margin of Qaidam basin. *Geol. Bull. China.* **2003**, *22*, 28–31. (In Chinese with English Abstract)
42. Liang, X.Q.; Fu, J.G.; Wang, C.; Jiang, Y.; Zhou, Y.; Yang, Y.Q.; Wang, Z.L.; Pan, C.C. Redefinition and formation age of the Tanjianshan group in Xitieshan region, Qinghai. *Acta Geol. Sin.* **2014**, *88*, 394–409. [[CrossRef](#)]
43. Li, F.; Wu, Z.L.; Li, B.Z.; Wang, L.F. Revision of the Tanjianshan Group on the northern margin of the Qaidam basin. *Northwest. Geol.* **2006**, *39*, 83–90. (In Chinese with English Abstract)
44. Fu, J.G.; Liang, X.Q.; Wang, C.; Jiang, Y.; Zhou, Y.; Pan, C.C.; Zhong, Y.S.; Yang, Y.Q.; Wang, Z.L. Timing and Characteristic of Provenance of the c Formation in the Tanjianshan Group, Xitieshan, North Qaidam. *Acta Geol. Sin.* **2014**, *88*, 1081–1092. (In Chinese with English Abstract)
45. Xu, Z.Q.; Yang, J.S.; Wu, C.L.; Li, H.B.; Zhang, J.X.; Qi, X.X.; Song, S.G.; Wan, Y.S.; Chen, W.; Qiu, H.J. Timing and Mechanism of Formation and Exhumation of the Qaidam Ultra-Pressure Metamorphic Belt. *Acta Geol. Sin.* **2003**, *77*, 163–176. (In Chinese with English Abstract)
46. Wang, M.J.; Song, S.G.; Niu, Y.L.; Su, L. Postcollisional magmatism: Consequences of UHPM terrane exhumation and orogen collapse, N. Qaidam UHPM belt, NW China. *Lithos* **2014**, *210*, 181–198. [[CrossRef](#)]
47. Zhao, Z.X. Paleozoic Tectono-Magmatic Evolution and Its Control on Lead-Zinc Mineralization in Xitieshan, North Qaidam. Ph.D. Thesis, China University of Geosciences, Wuhan, China, 2018. (In Chinese with English Abstract)
48. Leng, S.L. Geological Characteristics and Formation Mechanism of Two Types of Mineralization from Xitieshan Lead-Zinc Deposit, Qinghai Province. Master’s Thesis, China University of Geosciences, Wuhan, China, 2013. (In Chinese with English Abstract)
49. Zong, K.Q.; Klemd, R.; Yuan, Y.; He, Z.Y.; Guo, J.L.; Shi, X.L.; Liu, Y.S.; Hu, Z.C.; Zhang, Z.M. The assembly of Rodinia: The correlation of early Neoproterozoic (ca. 900 Ma) high-grade metamorphism and continental arc formation in the southern Beishan Orogen, southern Central Asian Orogenic Belt (CAOB). *Precambrian Res.* **2017**, *290*, 32–48. [[CrossRef](#)]
50. Liu, Y.S.; Hu, Z.C.; Gao, S.; Günther, D.; Xu, J.; Gao, C.G.; Chen, H.H. In situ analysis of major and trace elements of anhydrous minerals by LA-ICP-MS without applying an internal standard. *Chem. Geol.* **2008**, *257*, 34–43. [[CrossRef](#)]

51. Zhu, Z.Y.; Cook, N.J.; Yang, T.; Ciobanu, C.L.; Zhao, K.D.; Jiang, S.Y. Mapping of sulfur isotopes and trace elements in sulfides by LA-(MC)-ICP-MS: Potential analytical problems, improvements and implications. *Minerals* **2016**, *6*, 110. [[CrossRef](#)]
52. Keith, M.; Häckel, F.; Haase, K.M.; Schwarz-Schampera, U.; Klemm, R. Trace element systematics of pyrite from submarine hydrothermal vents. *Ore Geol. Rev.* **2016**, *72*, 728–745. [[CrossRef](#)]
53. Monecke, T.; Petersen, S.; Hannington, M.D.; Grant, H.; Samson, I. The minor element endowment of modern sea-floor massive sulfides comparison with deposits hosted in ancient volcanic successions. *Rev. Econ. Geol.* **2016**, *18*, 245–306.
54. Deditius, A.; Utsunomiya, S.; Reich, M.; Kesler, S.E.; Ewing, R.C.; Hough, R.; Walshe, J. Trace metal nanoparticles in pyrite. *Ore Geol. Rev.* **2011**, *42*, 32–46. [[CrossRef](#)]
55. Reich, M.; Deditius, A.; Chryssoulis, S.; Li, J.W.; Ma, C.Q.; Parada, M.A.; Barra, F.; Mittermayr, F. Pyrite as a record of hydrothermal fluid evolution in a porphyry copper system: A SIMS/EMPA trace element study. *Geochim. Cosmochim. Acta.* **2013**, *104*, 42–62. [[CrossRef](#)]
56. Thomas, H.V.; Large, R.R.; Bull, S.W.; Maslennikov, V.; Berry, R.F.; Fraser, R.; Froud, S.; Moye, R. Pyrite and pyrrhotite textures and composition in sediments, laminated quartz veins, and reefs at Bendigo gold mine, Australia: Insights for ore genesis. *Econ. Geol.* **2011**, *106*, 1–31. [[CrossRef](#)]
57. Reich, M.; Kesler, S.E.; Utsunomiya, S.; Palenik, C.S.; Chryssoulis, S.L.; Ewing, R.C. Solubility of gold in arsenian pyrite. *Geochim. Cosmochim. Acta* **2005**, *69*, 2781–2796. [[CrossRef](#)]
58. Huston, D.L.; Sie, S.H.; Suter, G.F.; Cooke, D.R.; Both, R.A. Trace elements in sulfide minerals from eastern Australian volcanic-hosted massive sulfide deposits; Part I, Proton microprobe analyses of pyrite, chalcopyrite, and sphalerite, and Part II, Selenium levels in pyrite; comparison with  $\delta^{34}\text{S}$  values and implications for the source of sulfur in volcanogenic hydrothermal systems. *Econ. Geol.* **1995**, *90*, 1167–1196.
59. Blanchard, M.; Alfredsson, M.; Brodholt, J.; Wright, K.; Catlow, C.R.A. Arsenic incorporation into FeS<sub>2</sub> pyrite its influence on dissolution: A DFT study. *Geochim. Cosmochim. Acta.* **2007**, *71*, 624–630. [[CrossRef](#)]
60. Reich, M.; Chryssoulis, S.L.; Deditius, A.; Palacios, C.; Zúñiga, A.; Welt, M.; Alvear, M. “Invisible” silver and gold in supergene digenite (Cu<sub>1.8</sub>S). *Geochim. Cosmochim. Acta.* **2010**, *74*, 6157–6173. [[CrossRef](#)]
61. Koglin, N.; Frimmel, H.E.; Minter, W.E.L.; Brätz, H. Trace-element characteristics of different pyrite types in Mesoarchean to Paleoproterozoic placer deposits. *Miner. Deposita* **2010**, *45*, 259–280. [[CrossRef](#)]
62. Genna, D.; Gaboury, D. Deciphering the hydrothermal evolution of a VMS system by LA-ICP-MS using trace elements in pyrite: An example from the Bracemac-McLeod deposits, Abitibi, Canada, and implications for exploration. *Econ. Geol.* **2015**, *110*, 2087–2108. [[CrossRef](#)]
63. Keith, M.; Smith, D.J.; Jenkin, G.R.T.; Holwell, D.A.; Dye, M.D. A review of Te and Se systematics in hydrothermal pyrite from precious metal deposits: Insights into oreforming processes. *Ore Geol. Rev.* **2018**, *96*, 269–282. [[CrossRef](#)]
64. Goodfellow, W.D. Geology and genesis of the Caribou deposit, Bathurst Mining Camp, New Brunswick, Canada. *Econ. Geol. Monogr.* **2003**, *11*, 327–360.
65. Kelley, K.D.; Leach, D.L.; Johnson, C.A.; Clark, J.L.; Fayek, M.; Slack, J.F.; Anderson, V.M.; Ayuso, R.A.; Ridley, W.I. Textural, Compositional, and Sulfur Isotope Variations of Sulfide Minerals in the Red Dog Zn-Pb-Ag Deposits, Brooks Range, Alaska: Implications for Ore Formation. *Econ. Geol.* **2004**, *99*, 1509–1532. [[CrossRef](#)]
66. Wohlgemuth-Ueberwasser, C.C.; Viljoen, F.; Petersen, S.; Vorster, C. Distribution and solubility limits of trace elements in hydrothermal black smoker sulfides: An in-situ LA-ICP-MS study. *Geochim. Cosmochim. Acta.* **2015**, *159*, 16–41. [[CrossRef](#)]
67. Craig, J.R.; Vokes, F.M.; Solberg, T.N. Pyrite: Physical and chemical textures. *Miner. Deposita* **1998**, *34*, 82–101. [[CrossRef](#)]
68. Marshall, B.; Gilligan, L.B. An introduction to remobilization: Information from ore-body geometry and experimental considerations. *Ore Geol. Rev.* **1987**, *2*, 87–131. [[CrossRef](#)]
69. Large, R.R.; Maslennikov, V.V.; Robert, F.; Danyushevsky, L.V.; Chang, Z. Multistage sedimentary and metamorphic origin of pyrite and gold in the giant Sukhoi Log deposit, Lena gold province, Russia. *Econ. Geol.* **2007**, *102*, 1233–1267. [[CrossRef](#)]
70. Agangi, A.; Hofmann, A.; Wohlgemuth-Ueberwasser, C.C. Pyrite Zoning as a Record of Mineralization in the Ventersdorp Contact Reef, Witwatersrand Basin, South Africa. *Econ. Geol.* **2013**, *108*, 1243–1272. [[CrossRef](#)]
71. Steadman, J.A.; Large, R.R.; Olin, P.H.; Danyushevsky, L.V.; Meffre, S.; Huston, D.; Wells, T. Pyrite trace element behavior in magmatic-hydrothermal environments: An LA-ICPMS imaging study. *Ore Geol. Rev.* **2020**, *128*, 103878. [[CrossRef](#)]
72. Ren, Y.Q.; Wohlgemuth-Ueberwasser, C.C.; Huang, F.; Shi, X.F.; Li, B.; Oelze, M.; Schreiber, A.; Wirth, R. Distribution of trace elements in sulfides from Deyin hydrothermal field, Mid-Atlantic Ridge—Implications for its mineralizing processes. *Ore Geol. Rev.* **2020**, *128*, 103911. [[CrossRef](#)]
73. Tauson, V.; Rychagov, S.; Akimov, V.; Lipko, S.; Smagunov, N.; Gerasomov, I.; Davletbaev, R.; Loginov, B. Role of surface phenomena in concentrating incompatible elements: Au in pyrite from hydrothermal clays at thermal fields in southern Kamchatka. *Geochem. Int.* **2015**, *53*, 973–986. [[CrossRef](#)]
74. Gregory, D.D.; Large, R.R.; Halpin, J.A.; Lounejeva Baturina, E.; Lyons, T.W.; Wu, S.; Sack, P.J.; Chappaz, A.; Maslennikov, V.V.; Bull, S.W.; et al. Trace element content of sedimentary pyrite in black shales. *Econ. Geol.* **2015**, *110*, 1389–1410. [[CrossRef](#)]
75. Large, R.R.; Halpin, J.A.; Danyushevsky, L.V.; Maslennikov, V.V.; Bull, S.W.; Long, J.A.; Gregory, D.D.; Lounejeva, E.; Lyons, T.W.; Sack, P.J. Trace element content of sedimentary pyrite as a new proxy for deep-time ocean–atmosphere evolution. *Earth Planet Sci. Lett.* **2014**, *389*, 209–220. [[CrossRef](#)]

76. Raymond, O.L. Pyrite composition and ore genesis in the Prince Lyell copper deposit, Mt Lyell mineral field, western Tasmania, Australia. *Ore Geol. Rev.* **1996**, *10*, 231–250. [[CrossRef](#)]
77. Liu, G.X.; Yuan, F.; Deng, Y.F.; Jowitt, S.M.; Sun, W.A.; White, N.C.; Yang, D.; Li, X.S.; Zhou, T.F.; Huizenga, J.M. The genesis of the Hehuashan Pb-Zn deposit and implication for the Pb-Zn prospectivity of the Tongling district, Middle-Lower Yangtze River metallogenic belt, Anhui Province, China. *Ore Geol. Rev.* **2018**, *101*, 105–121. [[CrossRef](#)]
78. Xiao, X.J.; Ni, P. Discussion of comparison of metallogeny for SEDEX and sedimentary-rework base metal deposits. *Contrib. Geol. Miner. Resour. Res.* **2000**, *15*, 238–245. (In Chinese with English Abstract)
79. Gemmell, J.B.; Large, R.R. Stringer system and alteration zones underlying the Hellyer volcanogenic massive sulfide deposit, Tasmania. *Econ. Geol.* **1992**, *87*, 620–649. [[CrossRef](#)]
80. Huston, D.L. Stable isotopes and their significance for understanding the genesis of volcanic-hosted massive sulfide deposits: A review. *Rev. Econ. Geol.* **1999**, *8*, 157–179.
81. Goodfellow, W.D.; Peter, J.M. Sulphur isotope composition of the Brunswick No. 12 massive sulphide deposit, Bathurst Mining Camp, New Brunswick: Implications for ambient environment, sulphur source, and ore genesis. *Can. J. Earth Sci.* **1996**, *33*, 231–251. [[CrossRef](#)]
82. Velasco, F.; Sanchez-Espana, J.; Boyce, A.J.; Fallick, A.E.; Saez, R.; Almodovar, G.R. A new sulphur isotopic study of some Iberian Pyrite Belt deposits: Evidence of a textural control on sulphur isotope composition. *Miner. Deposita* **1998**, *34*, 4–18. [[CrossRef](#)]
83. Maclellan, K.L.; Lentz, D.R.; Mcclenaghan, S.H. Petrology, Geochemistry, and Genesis of the Copper zone at the Brunswick No. 6 Volcanogenic Massive Sulfide Deposit, Bathurst Mining Camp, New Brunswick, Canada. *Explor. Min. Geol.* **2006**, *15*, 53–75. [[CrossRef](#)]
84. Bradshaw, G.D.; Rowins, S.M.; Peter, J.M.; Taylor, B.E. Genesis of the Wolverine Volcanic Sediment-Hosted Massive Sulfide Deposit, Finlayson Lake District, Yukon, Canada: Mineralogical, Mineral Chemical, Fluid Inclusion, and Sulfur Isotope Evidence. *Econ. Geol.* **2008**, *103*, 35–60. [[CrossRef](#)]
85. Barrie, C.T.; Hannington, M.D. Classification of volcanic-associated massive sulfide deposits based on host-rock composition. *Rev. Econ. Geol.* **1999**, *8*, 1–11.
86. Saez, R.; Pascual, E.; Toscano, M.; Almodóvar, G.R. The Iberian type of volcano-sedimentary massive sulphide deposits. *Miner. Deposita* **1999**, *34*, 549–570. [[CrossRef](#)]
87. Wills, A.O.; Lentz, D.R.; Roy, G. Chemostratigraphy at the Brunswick No. 6 volcanic-sediment-hosted massive sulfide deposit, New Brunswick: Resolving geometry from drill core in deformed felsic volcanic rocks. *Explor. Min. Geol.* **2006**, *15*, 35–51. [[CrossRef](#)]
88. Shanks, W.C., III; Bischoff, J.L.; Rosenbauer, R.J. Seawater sulfate reduction and sulphur isotope fractionation in basaltic systems: Interaction of seawater with fayalite and magnetite at 200–350 °C. *Geochim. Cosmochim. Acta.* **1981**, *45*, 1977–1996. [[CrossRef](#)]
89. Rye, O.R.; Ohmoto, H. Sulfur and carbon isotopes and ore genesis: A review. *Econ. Geol.* **1974**, *69*, 826–842. [[CrossRef](#)]

**Disclaimer/Publisher’s Note:** The statements, opinions and data contained in all publications are solely those of the individual author(s) and contributor(s) and not of MDPI and/or the editor(s). MDPI and/or the editor(s) disclaim responsibility for any injury to people or property resulting from any ideas, methods, instructions or products referred to in the content.